Neutrino Transport in Core-Collapse Supernovae

An investigation of neutrino interactions and energetics in core-collapse supernovae
Master-Thesis von Paul Mekhedjian aus Darmstadt
Tag der Einreichung:

1. Gutachten: Prof. Dr. Almudena Arcones
2. Gutachten: Dr. Albino Perego

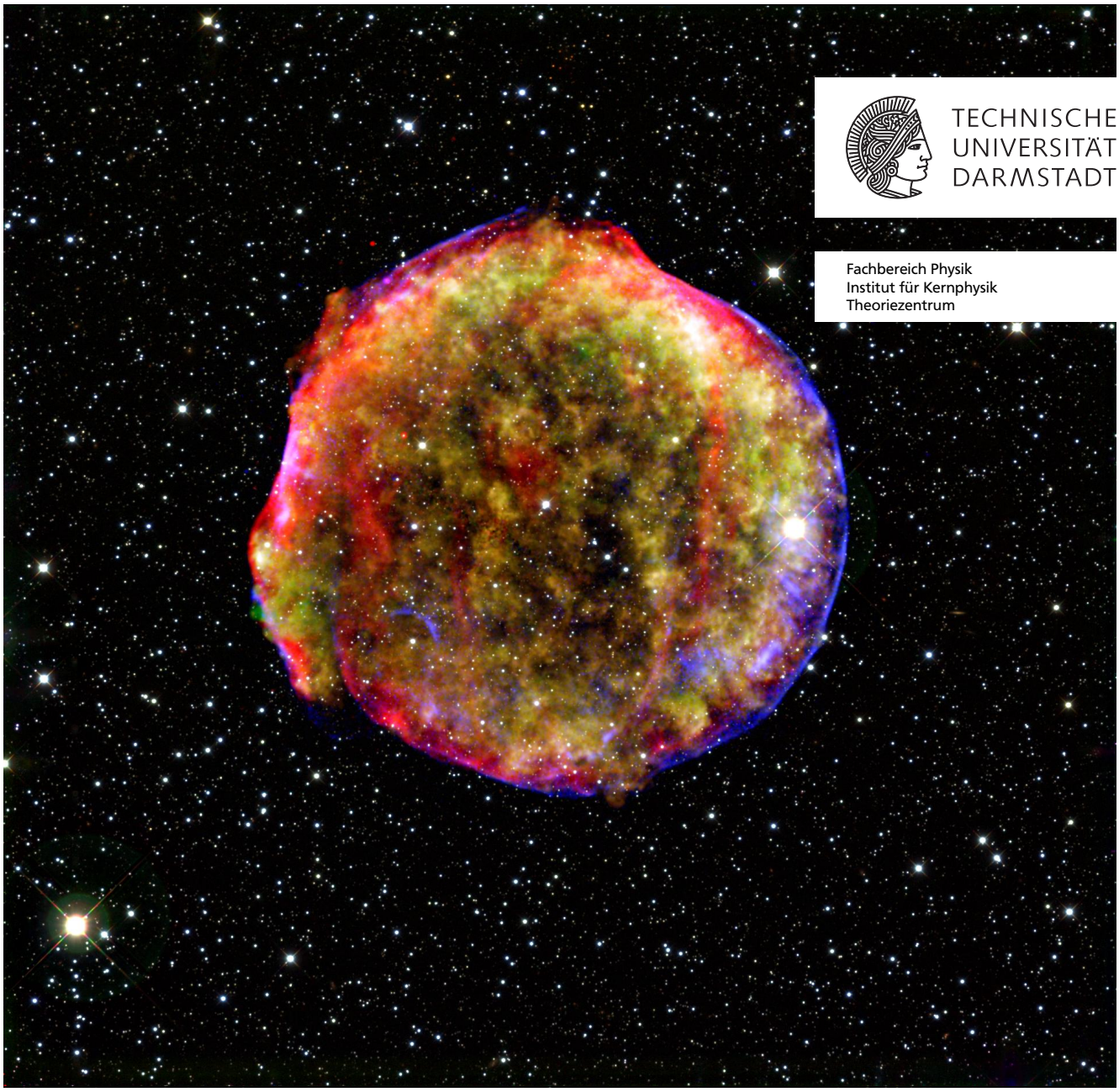

TECHNISCHE UNIVERSITÄT DARMSTADT

Fachbereich Physik
Institut für Kernphysik
Theoriezentrum

Neutrino Transport in Core-Collapse Supernovae
An investigation of neutrino interactions and energetics in core-collapse supernovae

Vorgelegte Master-Thesis von Paul Mekhedjian aus Darmstadt

1. Gutachten: Prof. Dr. Almudena Arcones
2. Gutachten: Dr. Albino Perego

Tag der Einreichung:

Erklärung zur Master-Thesis

Hiermit versichere ich, die vorliegende Master-Thesis ohne Hilfe Dritter nur mit den angegebenen Quellen und Hilfsmitteln angefertigt zu haben. Alle Stellen, die aus Quellen entnommen wurden, sind als solche kenntlich gemacht. Diese Arbeit hat in gleicher oder ähnlicher Form noch keiner Prüfungsbehörde vorgelegen.

Darmstadt, den October 15, 2014

(P. Mekhedjian)

Abstract

Core collapse supernovae are the dramatic death of massive stars, and at the same time the birth of some of the most extreme objects in the Universe, namely neutron stars. Due to the extreme conditions of density and temperature experienced during the collapse of a stellar core into a proto-neutron star, the released gravitational energy ($\sim 10^{53}$ erg) is carried away mainly by neutrinos, on a timescale of $\sim$10 s. The subtle balance between neutrino absorption and emission above the surface of the accreting proto-neutron star is thought to influence the explosion mechanism of a core-collapse supernova (neutrino-driven explosion mechanism), and to set the ratio between neutrons and protons in the expanding ejecta, which is crucial for the subsequent nucleosynthesis. The modeling of neutrino transport in such thermodynamical conditions is extremely challenging, especially for multi-dimensional numerical simulations. To tackle this problem, a large number of approximated transport schemes have been developed over the last few years.

In this thesis we have developed a new and efficient grey treatment for electron neutrinos and anti-neutrinos in the post-bounce phases of a core-collapse supernova. The new scheme has been developed in a post processing fashion, using the radial profiles of the thermodynamical quantities of a spherical symmetric core-collapse model of a 15 $M_{\odot}$ progenitor star, obtained by the open source Agile-IDSA code. After having determined the location of the neutrinospheres, we have computed consistently the radial profiles of the neutrino luminosities in the free-streaming regime, considering both emission and absorption processes. At the inner boundary condition of the neutrinospheres, we have assumed black-body neutrino emission. The electron fraction and the internal energy variations due to neutrinos have been calculated from the radial derivatives of the neutrino luminosities. Inside the neutrinosphere, a simple diffusion prescription is assumed.

A direct comparison of the results obtained by our scheme and the Agile-IDSA code reveals that we are able to reproduce the major features of neutrino transport, both in terms of local source terms and of temporal evolution of the luminosities at infinity. The outlook of this project is the direct implementation of our scheme into an existing hydrodynamics code, to model long-term evolution of a core-collapse supernova model.

Contents

1 Introduction to Core-Collapse Supernovae (CCSNe)

1.1 Observation & Experiment

As supernovae occur readily throughout our universe, they have also been observed using modern scientific instrumentation. Emission of light from supernovae and its strength can be tracked over time to create plots such as the one in Figure 1. These plots have been able to show that photon emission from radioactive decay of certain elements can last months and even upwards of a year or two for some supernovae. The total energy of a core-collapse supernova is proportional to its total gravitational binding energy: $E_{SN} \propto GM_{NS}^2/R_{NS} \sim 10^{53}$ erg (where M_{NS} and R_{NS} are the mass and radius of the forming neutron star, respectively). Roughly 1% ($\sim 10^{51}$ erg) of that binding energy is transferred to the explosion energy and of that, only 0.1% - 0.01% ($\sim 10^{49}$ erg) is manifest in the visual light spectrum (LeVeque et al. [1997]). The rest of the original gravitational binding energy ($\sim$ 99%!) is thought to be carried away by neutrinos in the seconds following a supernova explosion.

Generally speaking, a measured photon flux (on Earth or a detector in orbit) is related to the intrinsic luminosity L_γ of the object of interest by :

$$F_\gamma = \frac{L_\gamma}{4\pi r^2} \quad \Rightarrow \quad L_\gamma = 4\pi r^2 \cdot F_\gamma \tag{1}$$

where F_γ is the photon flux and r is the distance to the object in question from the observatory.

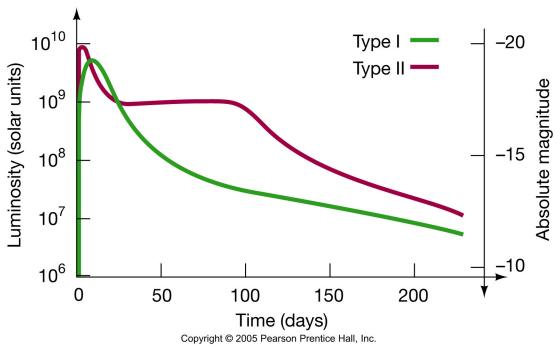

Figure 1: Light Curve Comparison

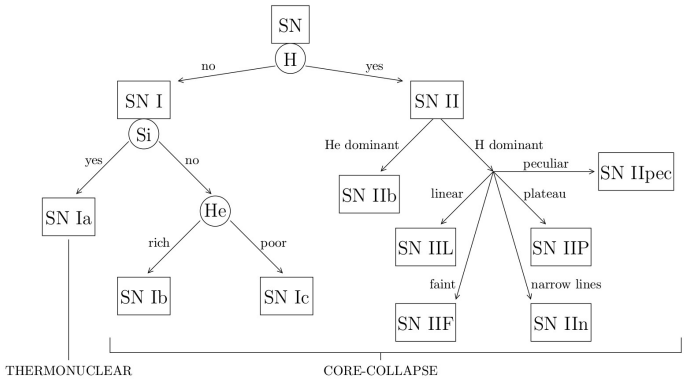

Figure 2: SN Taxonomy: Raffelt [2012]

These celestial displays of violent magnitude may be generally classified into two types (I or II) based on their spectral emission content. Type I supernovae lack the presence of hydrogen (H) lines, whereas type II supernovae include them. The disparity in the light curves (as shown in Figure 1) illustrates the fact that different isotopic decay processes (which emit γ rays, X rays, UV rays and visual light) dominate at some intervals of time and suffer at others.

This classification, however, does not reflect the different explosion mechanisms behind the supernovae. Types I and II may be further subdivided into more specific categories (see Figure 2), where Type Ia supernovae explode in a thermonuclear explosion and types Ib, Ic, and type II explode in the form of a core-collapse supernova (CCSN). In this work, we will focus specifically on supernovae of the latter type, ignoring the mechanism behind Type Ia supernovae. Through the course of this work, we will better understand the physical mechanisms which trigger (Type II) CCSNe, the proto-neutron stars which they leave in their wake immediately after the explosion, and what sets their originating stars or *progenitors* apart from other stars througout the universe.

SN 1987A

What is most shocking about supernova explosions is best illustrated by the case of SN 1987A. SN 1987A was a CCSN which occurred approximately 160,000 light years away from Earth, outside of our own galaxy in the Large Magellanic Cloud (a galactic neighbor to the Milky Way). The progenitor, Sanduleak (Sk) 69 202, is currently thought to have been a 20 $M_\odot$ at its zero-age main sequence (ZAMS) evolutionary phase.

The incident neutrino flux from SN 1987A on Earth (with respective energies depicted in Figure 4) was on the order of 10^8 neutrinos/(cm$^2 \cdot$ s), which is relatively[1] high compared to that of the solar neutrino flux, which has a value close to 10^{10} neutrinos/(cm$^2 \cdot$s). A total of 25 neutrinos were detected from the neutrino emission, lasting no more than 10-12 seconds (consistent with the Kelvin-Helmholtz timescale of proto-neutron star cooling). Observations from this event

[1] the Sun is only 1 AU (astronomical unit) in distance from the Earth, whereas SN 1987A $\approx 10^{10}$ AU away.

Figure 3: SN 1987A in Visible Light Range
(ESA/Hubble & NASA)

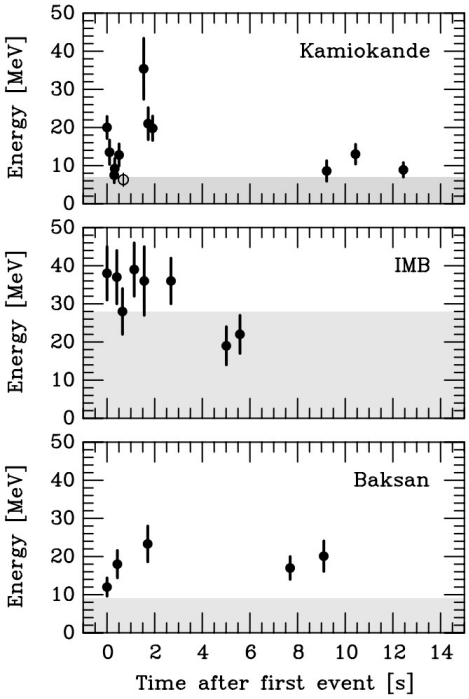

Figure 4: Energy vs. Time of Events
Raffelt [2012]

were made by neutrino detectors at Kamiokande II (in Japan), Irvine-Michigan-Brookhaven (in the United States), and the Baksan Neutrino Observatory (in Caucasian Russia).

Although photons move at the speed of light, neutrinos, due to their finite mass, are sub-luminal. In SN 1987A, neutrinos were observed approximately 3 hours *before* photons. The reason behind this will be explained in a later section, but is at first glance, rather surprising and counter-intuitive. Neutrino detection is also limited by matter interaction cross sections and detectors of finite size may only detect a tiny fraction of incident neutrinos. This is why so few neutrinos were actually detected.

Though only theorized to occur within our own galaxy once every 30-50 years, the quality of the data coming from these particular, closer supernovae are expected to be better, due to the higher neutrino flux on account of this proximity (recall $F_\nu = L_\nu/4\pi r^2$, now for neutrinos ν) and due to the many advancements in neutrino detection sensitivity and precision since the late 1980s. With this in mind, the future of neutrino physics is rather bright and will benefit from the next detectable supernova.

1.2 Physical Models Behind Core-Collapse Supernovae

1.2.1 Neutrino Theory

As alluded to in Section 1.1, neutrinos play a very important role in core-collapse supernovae (CCSNe). Up to 99% of the energy emitted (originally in the form of gravitational binding energy) in a supernova explosion is in the form of neutrinos. How can they possibly be so effective at taking energy away from a system? In order to assess the extent of this role, it is best to take a deeper look into how these unique particles are characterized, formally introduce some concepts, and then explain how and why neutrino transport plays as strong a role as it does in the proto-neutron star environment.

Neutrinos, like electrons, are **fermions**. Unlike the electrons, muons and tauons with which they are related, neutrinos have **no electric charge** (see Table 1). After the first postulation of neutrinos by Wolfgang Pauli in 1930, it was theorized that they, as fermions, are particles which follow Fermi-Dirac statistics and obey the Pauli Exclusion Principle. The most commonly encountered in introductory physics texts is the electron neutrino ν_e. Under the Dirac interpretation of neutrinos and assuming a massless chiral field (see Chapter 2, Giunti and Kim [2007]), this particle also has its own anti-particle: the electron antineutrino $\bar{\nu}_e$. The various neutrino species, as well as their related fermions and characteristic lepton numbers, are summarized in Table 1. Neutrinos which are capable of interacting with matter can interact in one of two ways:

Neutral Current Interactions (Z Boson Mediation): In the case of neutral current (NC) interactions, we consider two types of neutrino-nucleon scattering (in the fashion of Bilenki [1982] and Bruenn [1985]):

- Elastic scattering (e.g. Scattering off nuclei during core collapse: $\nu + N \rightleftharpoons \nu + N$): Conservative
- Inelastic scattering (e.g. Neutrino thermalization by scattering off electrons: $\nu + e^{\pm} \rightleftharpoons \nu + e^{\pm}$): Non-conservative

Charged Current Interactions ($W^{\pm}$ Boson Mediation): With the case of charged current (CC) interactions, the $W^{\pm}$ boson mediates the conversion of a quark in a hadron and converts the incident neutrino to an electron, or vice versa in the inverse reaction. Examples are shown below:

$$\left.\begin{array}{rcl} \mathrm{e}^- + \mathrm{p} & \rightleftharpoons & \mathrm{n} + \nu_e \\ \mathrm{e}^+ + \mathrm{n} & \rightleftharpoons & \mathrm{p} + \bar{\nu}_e \end{array}\right\} \quad \mathrm{e}^{+/-}\ \text{Capture}$$

$$\left.\begin{array}{rcl} {}^{\mathrm{A}}_{\mathrm{Z}}\mathrm{N} \longrightarrow {}^{\mathrm{A}}_{\mathrm{Z+1}}\mathrm{N}' + \mathrm{e}^- + \nu_e & \Longrightarrow & {}^{137}_{55}\mathrm{Cs} \longrightarrow {}^{137}_{56}\mathrm{Ba} + \mathrm{e}^- + \bar{\nu}_e \\ {}^{\mathrm{A}}_{\mathrm{Z}}\mathrm{N} \longrightarrow {}^{\mathrm{A}}_{\mathrm{Z-1}}\mathrm{N}' + \mathrm{e}^+ + \bar{\nu}_e & \Longrightarrow & {}^{22}_{11}\mathrm{Na} \longrightarrow {}^{22}_{10}\mathrm{Ne} + \mathrm{e}^+ + \nu_e \end{array}\right\} \quad \beta^{+/-}\ \text{Decay}$$

For the sake of consistency, references to neutrinos in general will be made hereafter using the ν symbol, with usage of ν_x being reserved for $\nu_x = \{\nu_\mu, \nu_\tau, \bar{\nu}_\mu, \bar{\nu}_\tau\}$ (as these heavier neutrinos may be aggregately characterized). It is worth mentioning that the neutrino spectrum from supernovae, in particular the neutrino burst, is primarily composed of electron neutrinos ν_e (due to pre-collapse/collapse phase electron capture), the luminosity[2] of which in a core-collapse supernova is typically (depending on the mass and size of the dying star) on the order of 300 ± 100 B/s. Electron anti-neutrinos $\bar{\nu}_e$ and more energetic neutrino species ν_x are not produced until the post-bounce phase of core-collapse.

Table 1: Leptonic Properties

Species	Charge	Lepton Number
e^- / e^+	-1/+1	+1/-1
μ^- / μ^+	-1/+1	+1/-1
τ^- / τ^+	-1/+1	+1/-1
$\nu_e / \bar{\nu}_e$	0/0	+1/-1
$\nu_\mu / \bar{\nu}_\mu$	0/0	+1/-1
$\nu_\tau / \bar{\nu}_\tau$	0/0	+1/-1

Table 2: Charged-Current Interactions

Nuclear Interaction	Type	Reaction
$p + e^- \rightleftharpoons n + \nu_e$	Capture	I
$n + e^+ \rightleftharpoons p + \bar{\nu}_e$	Capture	II
$e^- + (A, Z) \rightleftharpoons (A, Z-1) + \nu_e$	Capture	III
$e^+ + (A, Z) \rightleftharpoons (A, Z+1) + \bar{\nu}_e$	Capture	IV

Table 3: Neutral Current Interactions

Nuclear Interaction	Type	Reaction
$\nu + N \rightleftharpoons \nu + N$	Scattering	V
$N + N \rightleftharpoons N + N + \nu + \bar{\nu}$	Bremsstrahlung	VI
$\nu + (A, Z) \rightleftharpoons \nu + (A, Z)$	Scattering	VII
$\nu + e^{\pm} \rightleftharpoons \nu + e^{\pm}$	Scattering	VIII
$\nu + (A, Z) \rightleftharpoons \nu + (A, Z)^*$	Scattering	IX
$e^+ + e^- \rightleftharpoons \nu + \bar{\nu}$	Pair Production	X
$(A, Z)^* \rightleftharpoons (A, Z) + \nu + \bar{\nu}$	De-Excitation	XI
$\nu_e \bar{\nu}_e \rightleftharpoons \nu_{\mu,\tau} \bar{\nu}_{\mu,\tau}$	Inter-Neutrino	XII

[2] where 1 B (in honor of Hans Bethe) is equal to 10^{51} erg

Heavy Neutrinos: In addition to ν_e and $\bar{\nu}_e$, there also exist two additional *species* or *generations* of neutrinos, known as muon and tau neutrinos ν_μ and ν_τ, each with its own respective antiparticle $\bar{\nu}_\mu$ and $\bar{\nu}_\tau$. In supernovae, ν_μ and ν_τ are produced by neutral current (NC) reactions, such as bremsstrahlung, among other processes. Since they decouple deeper in the proto-neutron star environment, these heavy neutrinos tend to have a more energetic profile than ν_e and $\bar{\nu}_e$ neutrinos. Other examples include:

$$\left.\begin{aligned} e^- + e^+ &\longrightarrow \nu_\mu + \bar{\nu}_\mu \\ e^- + e^+ &\longrightarrow \nu_\tau + \bar{\nu}_\tau \end{aligned}\right\} \quad \text{Thermal Pair Production}$$

The aforementioned concepts and defined quantities will be used throughout this work and the following sections, in which we describe the defining moment of the core-collapse phase. In this regime, neutrinos begin to affect the landscape of the core-collapse system. As matter compresses, density rises, and the mean free path is then on the same order of magnitude as the radius of the proto-neutron star, and will continue to become smaller until the neutrino mean free path greatly reduces and their en masse movements lead to interesting dynamical effects. Tables 2 and 3 summarize all the potential weak-force mediated nuclear reactions which can affect the energetics of a supernova in its various stages of evolution.

1.2.2 Massive Star Evolution

For stars more massive than $M \gtrsim 8\ M_\odot$, nuclear burning through the CNO cycle proceeds past various stages (C, Ne, O, Si burning), by both nuclear fusion and photodissociated quasi-equilibrium α captures (described in Woosley et al. [2002]). Burning timescales for hydrogen, helium and carbon well surpass human lifetimes, with each successive burning stage becoming drastically shorter: H-burning on the order of millions of years, He-burning for hundreds of thousands, C-burning for hundreds, and Ne- and O-burning for just months! The time frame leading up to the iron core is then an astronomical instant, with Mg-burning lasting roughly a week and Si burning only lasting about a day!

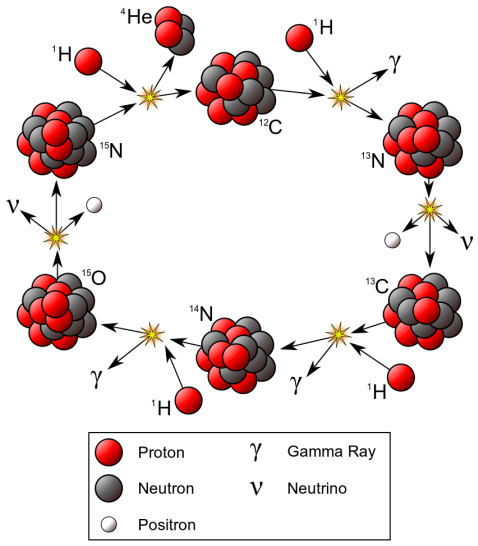

Figure 5: CNO Cycle: Nuclear Burning in Massive Stars

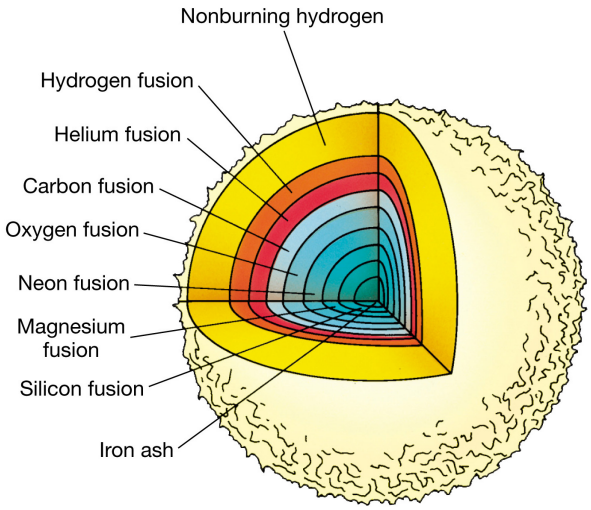

Figure 6: Burning Layer Stratification

1.2.3 Chandrasekhar Mass, Collapse, Bounce and Post-Bounce Phases

As a consequence of Si burning, the core is then composed of iron and iron-group nuclei (shown in blue in Figure 6), whilst shells of greater radii continue to burn lighter nuclei. This is the essence of the so called *onion-ring structure*. Although from its exterior the star looks like a red giant, the inner core of a massive star just prior to core-collapse (for these more massive stars) resembles that of a white dwarf. Coincidentally, both stellar cores (of a white dwarf and a pre-CCSNe iron core) are supported against collapse by a force provided by the gradient pressure from **degenerate electrons**.

Chandrasekhar Mass M_{ch}

Subrahmanyan Chandrasekhar, a world-renowned astrophysicist from the early 20th century, showed that there is a maximum stellar core mass allowable by relativistic, degenerate electrons. If such a stellar core configuration (which

happens to be the kind we are considering) were to ever reach this particular mass, he postulated that the force of gravity would supercede the degenerately-induced, collective force of electrons on an exponentially reactive timescale. This phenomenon is known as **core collapse**. Aside from raw baryonic matter (manifested in $M_\odot$), this value for the Chandrasekhar mass is dependent on the value of the electron fraction Y_e, which is defined as:

$$\left.\begin{aligned} Y_\mathrm{e} = \frac{n_e}{\rho \cdot N_A} = \frac{n_e}{n_\mathrm{baryon}} = \frac{n_p}{n_p + n_n} \end{aligned}\right\} \quad n_e = n_p \text{ by charge neutrality}$$

where n_i = number density of species i in either free or bound states, and $N_A \equiv$ Avogadro's number $\left(= 6.022 \times 10^{23}/\mathrm{g}\right)$. This particular quantity Y_e will appear quite often in this work and determines the *number of electrons per number of baryons* in an environment. In **neutron-rich** matter $Y_\mathrm{e} < 0.5$, whereas in **proton-rich** matter, $Y_\mathrm{e} > 0.5$. $Y_\mathrm{e} = 0.5$ is the line of demarcation (and equality of number of species) between these regimes. The Chandrasekhar mass (along with its dependence on Y_e) is given by:

$$M_\mathrm{ch} \simeq 5.83 \cdot Y_\mathrm{e}^2 \cdot M_\odot$$

The iron core is composed of iron nuclei conducting a plasma of highly-degenerate, relativistic Fermi electrons. Prior to reaching the Chandrasekhar mass (where $M_\mathrm{core} < M_\mathrm{ch}$), M_core typically has values of $\rho_c \approx 10^9$ g/cm^3, $T_c \approx (8 - 10) \times 10^9$ K and $Y_\mathrm{e} \approx 0.42 - 0.44$. This makes sense, because just prior to collapse, Y_e is already continually decreasing ($Y_\mathrm{e} \downarrow$ yields $M_\mathrm{ch} \downarrow$) due to electron capture on nuclei via:

$$e^- + (A, Z) \rightarrow (A, Z-1) + \boldsymbol{\nu_e}$$

Collapse Phase

During the aforementioned electron capture, Si-shell burning continues and causes M_core to increase. At the onset of collapse, the satisfaction of $M_\mathrm{core} = M_\mathrm{ch}$ triggers the gravitational instability described by Chandrasekhar. Here, radial velocity $\vec{v}$ is < 0, collapsing matter gravitationally to the center of the core. As ρ_c increases, the **electron chemical potential** μ_e also increases, related by $\mu_e(\rho) = \rho^{1/3}$ (as derived in Bethe [1990]). This increase in μ_e facilitates electron capture onto nuclei, accelerating **deleptonization** further. Electron capture onto free protons proceeds by:

$$e^- + p \rightarrow n + \boldsymbol{\nu_e}$$

Neutrons and neutrinos are by-products of this reaction and the phase of **deleptonization** accelerates more steadily. As electrons are actively consumed in this process, the electron abundance $\mathrm{Y_e}$ also drops. Core collapse is a two-fold process, with the structurally sustaining force of electron pressure decreasing due to the continuous disappearance of electrons (i.e. due to the value of $\mathrm{Y_e}$ decreasing).

The collapse timescale of the stellar core after surpassing M_ch is given by:

$$\boxed{t_\mathrm{collapse} \simeq \frac{1}{\sqrt{\mathrm{G} \cdot \rho_c}}} \tag{2}$$

where ρ_c is the characteristic density of the core and the gravitational constant $\mathrm{G} \equiv 6.67 \times 10^{-8}$ cm^3/g$\cdot$s^2. For example:

$$\rho_c = 10^9 \text{ g/cm}^3 \longrightarrow \underline{t_\mathrm{collapse} \simeq 120 \text{ ms}}$$

In later phases of collapse (approaching $\rho_c \approx 10^{12}$ g/cm^3), electron neutrinos $\boldsymbol{\nu_e}$ released from electron capture stream away. Upon surpassing $\rho_c \gtrsim 3 \times 10^{12}$ g/cm^3, during material infall, neutrinos become **trapped**, with the **electron neutrino fraction** Y_{ν_e} growing from a pre-collapse value of $Y_{\nu_e} \approx 10^{-5} - 10^{-4}$ to a value of $Y_{\nu_e} \approx 0.08 - 0.10$.

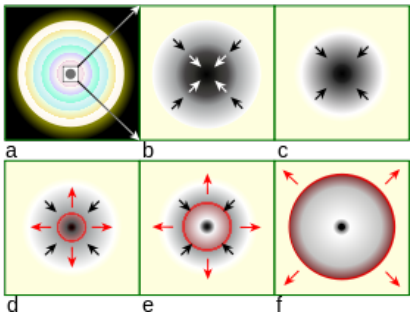

Figure 7: Collapse, Bounce, and Post-Bounce Shock (Source: Wikipedia Commons)

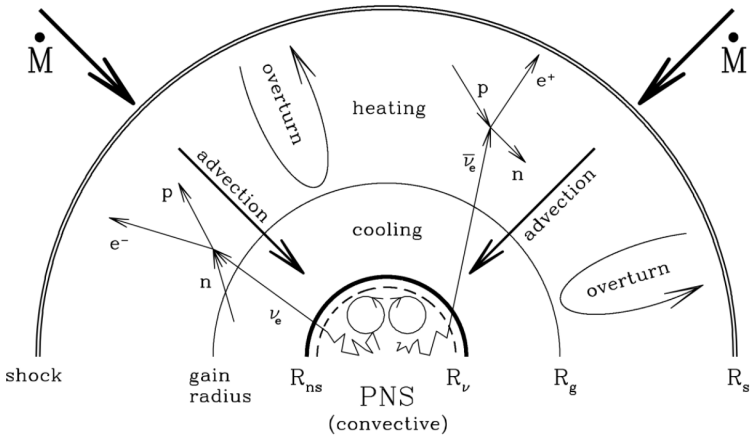

Figure 8: The Post-Bounce PNS Environment Janka [2001]

Bounce Phase

As core collapse begins to force every layer of the Fe core into the center (as depicted in Figure 7b and 7c), ρ_c moves swiftly from 10^9 g/cm^3 to 10^{14} g/cm^3. This means that in less than one second, the density of the core has increased one hundred thousand fold! At about 0.16/fm^3 (or roughly $\rho_c \gtrsim 2.7 \times 10^{14}$ g/cm^3), a characteristic density known as **nuclear saturation density** is reached. Here, nucleons are compressed at the density at which neutrons and protons "touch" in a nucleus. The exact dynamics of what happens at this moment are not well understood, but it is theorized that the equation of state (EOS) describing matter, pressure, and its energetics *stiffens*. This EOS is currently an active field of research and many developments in neutron star physics are able to constrain certain parameters, effectively rejecting implausible or unphysical equations of state.

The proto-neutron star core now has a physical obligation to communicate its new state to its surroundings and begins to propagate this information at the local sound speed c_s determined by the medium density. The propagating information moves outward, accumulating pressure waves and creating an outward moving shock at the surface of what will soon be the proto-neutron star. While this is occurring, the rest of the collapsing star is not yet privy to what has occurred at the stellar core, and thus continues to collapse (as illustrated in Figure 7d and 7e).

Post-Bounce and Explosion

The aforementioned shock continues to travel outward, dissociating iron-group nuclei in its wake, as the movement of the shock through matter is a dissipative process. The shock expends approximately 8.8 MeV of energy per baryon dissociating an Fe atom (as shown in Bethe [1990]). At the same time, a huge flux of neutrinos have left the system after bounce and continue to emit quite hefty luminosities, taking energy away from the system. Both these phenomena together lead to a phenomenon known as **shock stalling**. It has been shown in various supernova simulations that shock stalling occurs 100-200 ms p.b. (post-bounce) at a radius of roughly 100-200 km. In the meantime, as shown in Figure 8, accreting matter $\dot{\mathrm{M}} = 4\pi r^2 \rho \vec{v}$, [Janka, 2001] continues to fall into the shock, dissociating even more iron-group nuclei.

Shock stalling is such a straight-forward consequence of the shock's propagation in the proto-neutron star environment, that even rudimentary 1D hydrodynamic simulations demonstrate stalling roughly 150-200 ms post bounce (see Figure 11f). Hans Bethe even speculated that it was more likely the case that successful (compare both successful and unsuccessful explosions in Figure 10) Type II supernovae explode through the *delayed* shock mechanism as opposed to the *prompt* shock mechanism. Indeed, even more advanced 2D and 3D simulations express this feature, but if so, then what *actually* causes the supernova shock (see Figure 7f) to move outward? Since the stunning images taken by telescopes today (Figure 3) show outward radial propagation of matter over time, then something must definitely be causing this to occur, and most modern works are actually in agreement that neutrinos may play a decisive role in this mechanism.

1.3 Brief Review of Modeling

Due to the iterative, time-dependent nature of solving the equations of hydrodynamics, thermodynamics and neutrino transport, the first supernova studies were only performed in 1D computationally by Colgate and White in the 1960s. Remotivated from a long lull by SN 1987A and the advent of newer astrophysics simulation algorithms, physicists in the 1990s and 2000s developed more complicated and involved simulations. It wasn't even until the early 1990s that physicists integrated accurate nuclear physics describing matter beyond a polytropic ideal gas (i.e. a *nuclear* equation of state). Work by Lattimer and Swesty in 1993 and Shen et al. in 1998, provided an extension to describe more accurate

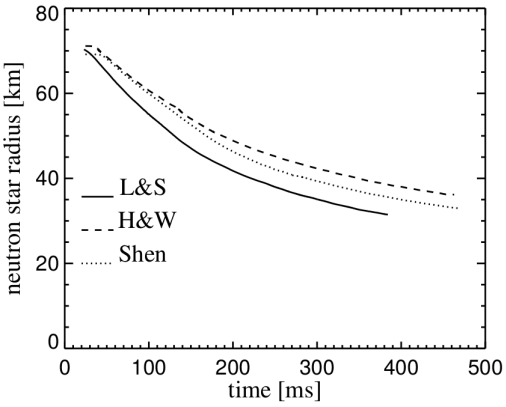

Figure 9: Proto-Neutron Star Surface vs. Time
Janka [2012]

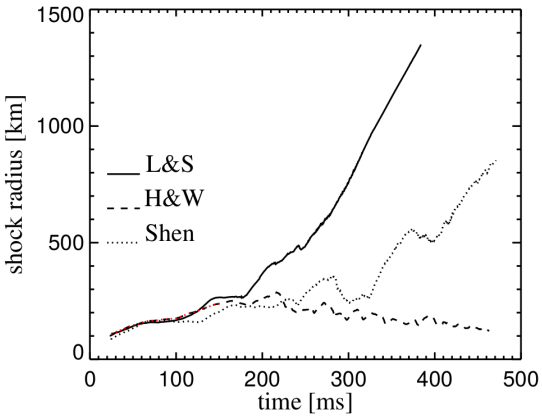

Figure 10: Shock Stalling vs. Shock Expansion
Janka [2012]

nuclear physics in higher densities, moving away from idealized assumptions which could not properly explain nuclear matter at high densities.

A crucial point to communicate to the reader is that one-dimensional (1D) simulations still continue to represent the most **accurate** physics, in spite of their dimensional limitation. Efforts to produce self-consistent 2D and 3D simulations have been good at best, but sometimes sacrifice some relevant microphysics to enable higher-dimensional computations. Between 2002 and 2005, many published works have incorporated and considered rather pioneering results in just one spatial dimension. Many supernova research groups have shown an impressive analysis of simulated emergent neutrino spectra of all known species, given neutral-current (NC) and charged-current (CC) nuclear interactions within core-collapse supernovae, and even considered neutrino flavor oscillations. It is in this sense that 1D simulations are the Occam's razor of supernova simulations.

In constrast, multi-dimensional simulations have shown that the future of supernova simulations must eventually move to a higher degree of spatial complexity. The failure to produce an explosion in almost all 1D simulations has motivated the thought that some physical effect or mechanism must still be missing. This is why more accurate multi-dimensional simulations have become necessary. One example of such an effect missing in 1D, the Standing Accretion Shock Instability (**SASI**), discovered by Blondin et al. [2003], showed in a 2D simulation that even the expanding shockwave may fall victim to multi-dimensional effects, asymmetrically swaying from pole to pole, whilst propagating outward. Other studies have confirmed that the SASI also exists in 3D. Another example, the **Rayleigh-Taylor instability**, is a rather common phenomenon in 3D fluid dynamics responsible for the turbulent mixing of fluids of various densities. Since the temperature gradients in the proto-neutron star environment trigger density stratification, copious amounts of self-similar Rayleigh-Taylor instabilities are generated within the proto-neutron star. Higher-resolution 3D simulations must be able to capture such microphysical effects. Indeed, it has also been shown that many features of **shock revival** (which causes the shock to recover from the stalling mentioned previously) find their origins in multi-dimensional thermodynamical convection and neutrino-induced lepton gradient convection. The reader is encouraged to look up the reviews by Janka [2012] and Burrows [2013] for an excellent summary of work already done and an outlook of upcoming developments.

1.4 Open Questions and What a Simulation Can Deliver

It is currently not fully understood what causes CCSNe to explode, as it has been shown by Arnett and Hillebrandt (see Bethe [1990]) in 1981 that the expanding shock wave loses most of its kinetic energy by dissociating heavy nuclei infalling towards the proto-neutron star surface. Many theories (as described in the previous section) have been proposed to explain what exactly revives the shock to a state where expansion is energetically plausible. Only the correct physics demonstrated in a self-consistent manner will be able to decisively determine the primary cause for a successful explosion and which other physical effects simply support or come secondary to it.

The specific goal of this thesis is to explore different degrees of freedom in a neutrino transport scheme for use in one- or multi-dimensional simulations of core-collapse supernovae. In this work, we use results from radiation transfer, hydrodynamics, and neutrino physics in order to define various quantities of interest, including: the neutrino mean free path, interaction cross section (for both absorption and scattering), opacity, optical depth, neutrino luminosity, and neutrino heating and cooling. To verify and corroborate these quantities, results from a numerical simulation are also presented in this work.

2 Theoretical Models, Computational Methods, & Luminosity Estimation Scheme

2.1 Agile-IDSA

Agile-IDSA is an (radially 1D, spherically-symmetric) implicit, general relativistic numerical code for modelling stellar collapse, bounce, and early post-bounce core collapse supernova evolution written by Matthias Liebendörfer at Universität Basel. It is this code whose output was used as a post-processing base for all the results presented in Section 3.

The code is actually an integration of two, already completed pieces of code: a separate hydrodynamics code (Agile: Liebendörfer et al. [2002]) and a neutrino transport code (IDSA: Liebendörfer et al. [2009]), which communicate with each other iteratively in time. The simulation allows for the toggling of the isotropic diffusion source approximation (IDSA) for neutrino transport, the (optional but recommended) usage of adaptive mesh refinement (AMR) in the radial grid, usage of general relativity as opposed to a pure Newtonian formulation of gravity, and toggling the effect of ν_μ and ν_τ annihilation and thermal pair production (i.e. yielding faster proto-neutron star cooling due to the emission of more energetic neutrinos), which plays a greater role in post-bounce energy evolution.

2.1.1 Hydrodynamics via Agile

Agile is an implicit time step hydrodynamics code which takes advantage of an adaptive radial grid for simulating specific applications which demand highly accurate, adaptive resolution. Non-equilibrium physics in space and time, such as in a shock wave, are a critical feature which must be handled very carefully and efficiently in Agile. The adaptive grid allows for greater resolution where it matters most to ensure physical discontinuities are treated as smoothly as possible. This criterion is thusly also perfect for the study of core-collapse supernovae.

With a smooth, reliable computational shock propagation mechanism in place, the hydrodynamics equations also require information about the proto-neutron star environment and the physics which can describe its self-interaction. The **equation of state** (EoS) is powerful construct which defines the physical state of matter at a wide range of densities, for both bound and dissociated matter. Since the pre-collapse PNS environment is typically described as an iron-core with pressure support provided by a degenerate electron gas, it is natural to want to model this system using a polytropic EoS. Here, pressure can be approximated as $P \propto \rho^\Gamma$ ($\Gamma = 5/3$ for a degenerate non-relativistic electron gas and $\Gamma = 4/3$ for a degenerate relativistic gas [Kippenhahn and Weigert, 1990]). This assumption and its corresponding inadequacy stems from the fact that the derivations of the formulae assume T=0. Even at high temperatures though, assuming partial degeneracy at finite temperatures does not capture the full microphysical, nuclear picture (especially at densities beyond **nuclear saturation**) and a **nuclear EoS** is necessary. Such an EoS assumes nuclear statistical equilibrium (NSE), alleviating the need for calculation of reaction rate networks for particles. Given simple inputs such as density ρ, temperature T and the number of electrons per nucleon Y_e, a uniquely described, closed state of matter may be described.

By default, Agile-IDSA uses the LS EoS (Lattimer and Douglas Swesty [1991]) to calculate empirical quantities assuming nuclear statistical equilibrium (NSE). It is a compressible liquid-drop model, which ensures a consistent transition between nuclei-dominated matter and that which cannot be described by a polytropic EoS at densities higher than 10^{12} g/cm^3. Values for species abundances Y_i, species chemical potentials μ_i, specific internal energy e, entropy s, pressure P may then be interpolated to meet any kind of condition which may exist in a plausible range of matter densities. Given initial conditions for a pre-collapse progenitor star, the EoS may then be called at every time step to compute all the necessary physical quantities for the rest of the simulation.

Deleptonization & Collapse

During early collapse, material in-fall is handled by Agile and no rigorous neutrino interactions are handled at this stage. As I introduced the pre-bounce collapse phase in Section 1.2.3, we also noted the importance of **deleptonization** in perpetuating the collapse, but this was dependent on a decreasing value of Y_e. Deleptonization is actually simulated using a simple parametrization routine (called DELEPT), as introduced and described in Liebendörfer [2005]. The subroutine provides a fit for $Y_e = Y_e(\rho)$ and IDSA then calculates the estimated pre-bounce neutrino luminosity $L_\nu^{\text{pre.b.}}$ based on the specific energy rate $\dot{e}$ and electron fraction change rate $\dot{Y}_e$ output received from the DELEPT module.

2.1.2 Neutrino Transport via IDSA

Neutrino transport in Agile-IDSA is handled by the **isotropic diffusion source approximation** (IDSA). Upon considering a particle distribution function f (in this case for neutrinos in the core-collapse supernova environment), IDSA decomposes this function f into two components: an isotropic distribution function of trapped particles f^{t} and a distribution function of streaming particles f^{s}. This allows for a state of superposition ($f = f^{\text{t}} + f^{\text{s}}$), allowing a representative state to be determined as a sum of both components, which undulate under conditions of local opacity[3]. Liebendörfer suggests an Ansatz to a particle transport equation $D(f = f^{\text{t}} + f^{\text{s}}) = C$, where D is a linear operator describing particle

[3] see Figure 3 in Liebendörfer et al. [2009]

propagation. $C = C^t + C^s$ is a decomposition of the corresponding collision integral for trapped and streaming particle components, respectively:

$$D\left(f^{\mathrm{t}}\right) = C^{\mathrm{t}} - \Sigma \tag{3}$$

$$D\left(f^{\mathrm{s}}\right) = C^{\mathrm{s}} + \Sigma \tag{4}$$

where Σ is defined as the **diffusion source**, which is responsible for converting *trapped* particles into *streaming* particles. This Ansatz may be kept in mind to relate the two components of the particle distribution function f.

Liebendörfer et al. [2009] then reveals the Boltzmann transport equation (BTE) (Equation 3 in their work) as the more complete analog to the aforementioned operator D. This equation describes the propagation of massless fermions moving at the speed of light c, and is traditionally used in rigorous treatments of neutrino transport in core-collapse supernova simulations, due to its completeness and its validity as an accurate model:

$$\frac{1}{c}\frac{df}{dt} + \mu\frac{\partial f}{\partial r} + \left[\mu\left(\frac{d\ln\rho}{cdt} + \frac{3v}{cr}\right) + \frac{1}{r}\right]\left(1-\mu^2\right)\frac{\partial f}{\partial \mu} + \left[\mu^2\left(\frac{d\ln\rho}{cdt} + \frac{3v}{cr}\right) - \frac{v}{cr}\right]E\frac{\partial f}{\partial E}$$

$$= j(1-f) - \chi f + \frac{E^2}{c\,(hc)^3}\cdot\left[(1-f)\int Rf'\,d\mu' - f\int R(1-f')\,d\mu'\right] \tag{5}$$

where f is the **neutrino distribution function** $f(t, r, \mu, E)$ as a function of time t, radius r, neutrino propagation angle μ and neutrino energy E, j is the **neutrino emissivity**, χ is the **neutrino absorptivity**, R is the isoenergetic elastic scattering kernel, ρ is the density of a compressible form of matter, and $(1-f)$ is the **Pauli blocking factor** explicitly expressed, assuming the identity $j(1-f) - \chi f = j - (j+\chi)f$. This form of the BTE is simpler than the one found in Bruenn [1985], as it ignores inelastic scattering and thermal pair production processes in the source terms at the right hand side of the equation. Additional source terms make the physical picture more accurate, but drastically increase the complexity of the coupled equations to be solved.

We recall the Ansatz and assume each component of f evolves separately according to Equation 5 and comment first on the trapped component f^{t}. Under the assumption of isotropy $f^{\mathrm{t}} = f^{\mathrm{t}}(t, r, E)$, Σ, and using the identity for Pauli blocking, angular integration of this equation yields (for f^{t} specifically):

$$\frac{df^{\mathrm{t}}}{c\,dt} + \frac{1}{3}\frac{d\ln\rho}{c\,dt}E\frac{\partial f^{\mathrm{t}}}{\partial E} = j - (j+\chi)f^{\mathrm{t}} - \Sigma \tag{6}$$

Through various assumptions and corrections to the bounds of the diffusion source (described in detail in Section 2 of Liebendörfer et al. [2009]), the diffusion source term Σ is finally expressed as:

$$\Sigma = \min\left\{\max\left[\alpha + (j+\chi)\frac{1}{2}\int f^{\mathrm{s}}d\mu, 0\right], j\right\}$$

$$\alpha = \frac{1}{r^2}\frac{\partial}{\partial r}\left(\frac{-r^2}{3(j+\chi+\phi)}\frac{\partial f^{\mathrm{t}}}{\partial r}\right)$$

where ϕ is the opacity due to isoenergetic scattering and the transport mean free path λ is thusly expressed as:

$$\lambda = 1/(j+\chi+\phi) \tag{7}$$

The *streaming* particle component f^{s} is then expressed in terms of an inertial laboratory frame as opposed to the fluid comoving frame used by the trapped component f^{t} previously (substituting $d\ln\rho/cdt = 0$ and $v = 0$ in Equation 5 for f^{s}). In addition, the particle energy terms are a constant of motion and are thus eliminated in this transformation:

$$\frac{\partial \hat{f}^{\mathrm{s}}}{c\partial \hat{t}} + \hat{\mu}\frac{\partial \hat{f}^{\mathrm{s}}}{\partial r} + \frac{1}{r}\left(1-\hat{\mu}^2\right)\frac{\partial \hat{f}^{\mathrm{s}}}{\partial \hat{\mu}} = -\left(\hat{j}+\hat{\chi}\right)\hat{f}^{\mathrm{s}} + \hat{\Sigma} \tag{8}$$

Then, due to the weakly coupling of the transformed source term $\hat{\Sigma}$ to $\hat{f}^{\mathrm{s}}$ and the relatively small size of $\hat{j}$ and $\hat{\chi}$ in the free-streaming domain, a stationary-state approximation is made to solve Equation 8. This drops the time-derivative

term on the left-hand side of the equation and if the sources on the right-hand side of Equation 8 are known, a Poisson equation for a potential ψ is recovered, whose gradient represents the particle flux:

$$\frac{\partial \psi}{\partial r} = \frac{1}{2}\int \hat{f}^{\mathrm{s}}\hat{\mu}\, d\hat{\mu} \tag{9}$$

$$\frac{1}{r^2}\frac{\partial}{\partial r}\left(r^2\frac{\partial \psi}{\partial r}\right) = \frac{1}{2}\int \left[-\left(\hat{j}+\hat{\chi}\right)\hat{f}^{\mathrm{s}} + \hat{\Sigma}\right] d\hat{\mu} \tag{10}$$

$$\frac{1}{2}\int \hat{f}^{\mathrm{s}}(E)\, d\hat{\mu} = \frac{2\,\frac{\partial \psi}{\partial r}(E)}{1+\sqrt{1-\left(\frac{R_\nu(E)}{\max(r,R_\nu(E))}\right)^2}} \tag{11}$$

where the final equation relates the flux to the streaming particle density (originally suggested by Bruenn in Liebendörfer et al. [2004]). R_ν is the radius of the neutrino scattering sphere, which depends on the neutrino energy E. The coupled quantities are then solved for and transformed from the laboratory frame to the comoving frame.

By relating a vector of variables U with a vector of corresponding fluxes F, Liebendörfer et al. [2009] goes on to present the Euler equation of mass conservation (traditionally expressed as $\partial\rho/\partial t + \nabla\cdot(\rho\vec{v}) = 0$) as:

$$\frac{\partial}{\partial t}U + \frac{\partial}{r^2\,\partial r}\left(r^2 F\right) = 0 \tag{12}$$

Rewriting Equation 6 in terms of the Eulerian time derivative and replacing the $d\ln\rho/dt$ term by velocity divergence yields:

$$\frac{df^{\mathrm{t}}}{c\,dt} + \frac{\partial}{r^2\,\partial r}\left(r^2\frac{v}{c}f^{\mathrm{t}}\right) + \frac{\partial}{r^2\,\partial r}\left(r^2\frac{v}{c}\right)\frac{\partial(E^3 f^{\mathrm{t}})}{3E^2\,\partial E} = j-(j+\chi)f^{\mathrm{t}}-\Sigma \tag{13}$$

IDSA then solves the advective part of Equation 13 alongside the hydrodynamic conservation law of Equation 12 using the following set of primitive variables:

$$U = \begin{pmatrix} \rho \\ \rho v \\ \rho(e+\frac{1}{2}v^2) \\ \rho Y_{\mathrm{e}} \\ \rho Y_l^{\mathrm{t}} \\ (\rho Z_l^{\mathrm{t}})^{\frac{3}{4}} \end{pmatrix}, \quad F = \begin{pmatrix} v\rho \\ v\rho v + p \\ v\rho(e+\frac{1}{2}v^2+\frac{p}{\rho}) \\ v\rho Y_{\mathrm{e}} \\ v\rho Y_l^{\mathrm{t}} \\ v\,(\rho Z_l^{\mathrm{t}})^{\frac{3}{4}} \end{pmatrix}$$

where p is the fluid pressure, e is the fluid specific internal energy, Y_{e} the electron fraction and l indicates the particle species of the trapped component. For the *trapped* component, the particle number fraction Y^{t} and particle mean specific energy Z^{t} may be calculated with:

$$Y^{\mathrm{t}} = \frac{m_{\mathrm{b}}}{\rho}\frac{4\pi}{(hc)^3}\int f^{\mathrm{t}}E^2\, dE\, d\mu \tag{14}$$

$$Z^{\mathrm{t}} = \frac{m_{\mathrm{b}}}{\rho}\frac{4\pi}{(hc)^3}\int f^{\mathrm{t}}E^3\, dE\, d\mu \tag{15}$$

Assuming a Fermi-Dirac distribution function for the trapped component of the distribution function f_l^{t} with free parameters β_l and μ_l expressed as $f_l^{\mathrm{t}}(E) = \{\exp[\beta_l(E-\mu_l)]+1\}^{-1}$, the change of the trapped component in time can be computed by:

$$\frac{\partial f_l^{\mathrm{t}}}{c\,\partial t} = j_l - (j_l+\chi_l)f_l^{\mathrm{t}} - \Sigma_l$$

This then leads to an equation for s_l, which Liebendörfer defines as the *net* interaction rate between matter and the radiation particles in question (neutrinos, in our case):

$$s_l = j_l - (j_l+\chi_l)f_l^{\mathrm{t}} + f_l^{\mathrm{s}} \tag{16}$$

And finally substituting and recovering additional useful forms:

$$s_l = \frac{\partial f_l^{\mathrm{t}}}{c\partial t} + \Sigma_l - (j_l + \chi_l)\frac{1}{2}\int f_l^s d\mu \tag{17}$$

$$\frac{\partial Y_{\mathrm{e}}}{c\,\partial t} = -\frac{m_{\mathrm{b}}}{\rho}\frac{4\pi c}{(hc)^3}\int (s_{\nu_e} - s_{\bar{\nu}_e})\,E^2\,dE \tag{18}$$

$$\frac{\partial e}{c\,\partial t} = -\frac{m_{\mathrm{b}}}{\rho}\frac{4\pi c}{(hc)^3}\int (s_{\nu_e} + s_{\bar{\nu}_e})\,E^3\,dE \tag{19}$$

These equations thusly allow for both energy gain and loss via $\dot{e}$ due to neutrino energy exchange with matter and changes to Y_{e}.

2.1.3 A Typical Model & Simulation Run

Now that Agile and IDSA have been explained, it is of interest to see them in action together, as Agile-IDSA. When a pre-supernova star progenitor profile is selected (either Woosley & Weaver 1995 or Woosley, Heger, & Weaver 2002), the program may be run with the option of toggling on or off cooling by heavy $\boldsymbol{\nu}_x$ neutrinos. For the rest of this work (and in this typical model), we consider only IDSA neutrino transport involving $\boldsymbol{\nu}_e$ and $\bar{\boldsymbol{\nu}}_{\boldsymbol{e}}$ absorption, emission and elastic scattering (as documented in Bruenn [1985], Appendix C):

Hydrodynamics Overview: Figures 11a-11f illustrate various hydrodynamic quantities plotted at five various times. These times capture the most definitive moments of proto-neutron star evolution:

- t_1: 0.5 ms p.b. - Captures the earliest moments immediately after the bounce which creates the outward propagating shock. A sharp discontinuity can be seen in all of the plots at this time which is the shock wave itself.
- t_2: 20 ms p.b. - The shock continues to propagate and burn through layers of the iron-core environment, dissociating iron and lighter nuclei in its wake. This act already begins the process of shock stagnation and successive stalling.
- t_3: 100 ms p.b. - The prompt shock nears its maximum (as seen in Figure 11f). Neutrino cooling and heating continue to exchange energy with matter in the gain region.
- t_4: 300 ms p.b. - Accreting matter continues to be dissociated (now falling in at higher velocity), causing a rise in entropy due to the proliferation of newly dissociated neutrons and protons, alongside the effects of neutrino heating.
- t_5: 600 ms p.b. - In the late cooling phase, neutrinos continue to cool the star further, yet do not provide enough energy via heating to revive the stalled shock. No additional dynamical effects can be seen as simulations reaches its stop criterion and ends shortly thereafter.

These times are laid out in Figure 11f (denoted by the orange stars) to illustrate their distribution throughout the elapsed time of the simulation. As one of the most tangible and easily understood quantities, we start this small discussion with that of density vs. radius. In Figure 11a at t_1, we note that the central density ρ_c is already at 2×10^{14} g/cm^3 , the nuclear saturation density. This is five orders of magnitude **greater** than the pre-collapse, progenitor core density of 10^9 g/cm^3. At about 20 km, there is a sharp drop in density which represents the transition between the stiffened, less compressible nuclear matter and all the matter outside of it. This represents the outwardly moving shock propagation front. It's important to note that this front does not start in the center of the star, but rather at the surface of the proto-neutron star (i.e. the surface of the homologous core).

At t_2 and t_3, the shock has traveled in time, to roughly 100 km and 200 km, keeping denser matter behind it and less dense matter in front of it. During this time, in-falling stellar matter continues to accrete onto the surface of the shock wave front, not yet privy to the nuclear state of matter inside the shock radius R_s, essentially feeding the growing baryonic density into the PNS. Thanks to Agile's adaptive mesh grid, the shock wave can be resolved very accurately, without causing erroneous results.

Times t_4 and t_5 represent later stages of evolution, with a tendency of strong density stratification starting to build after continued deleptonization. After 10-20 seconds, one would expect an extremely dense compact remnant of size 10-12 km (the neutron star itself) with very little non-accreted matter remaining outside of this radius.

Congruently, Figure 11b corroborates much of what has been said. Time t_1 shows a positive velocity front pushing against a front with higher velocity in-fall. This says something about the energy of the shock front created by the bounce

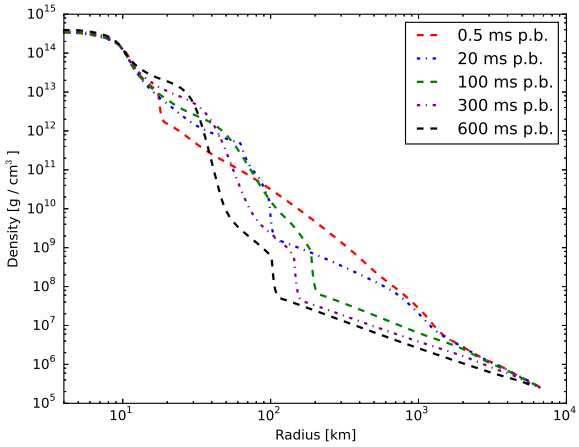

(a) Density vs. Radius

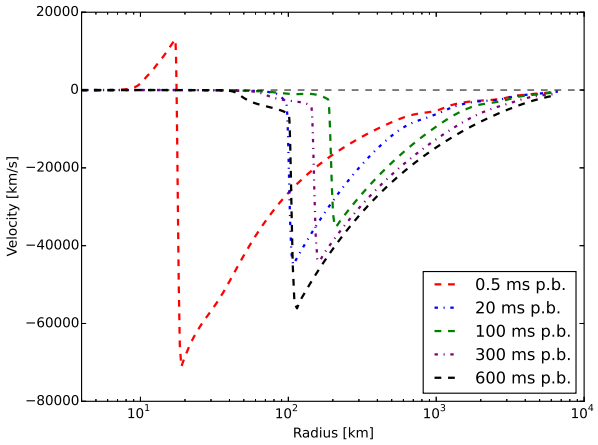

(b) Velocity vs. Radius

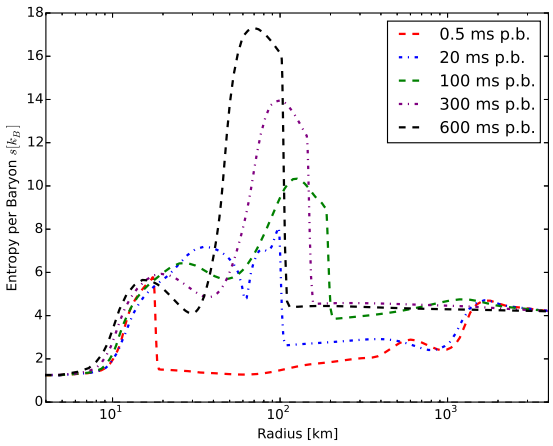

(c) Entropy vs. Radius

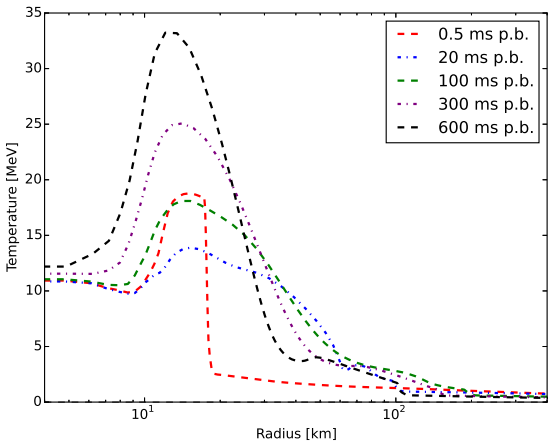

(d) Temperature vs. Radius

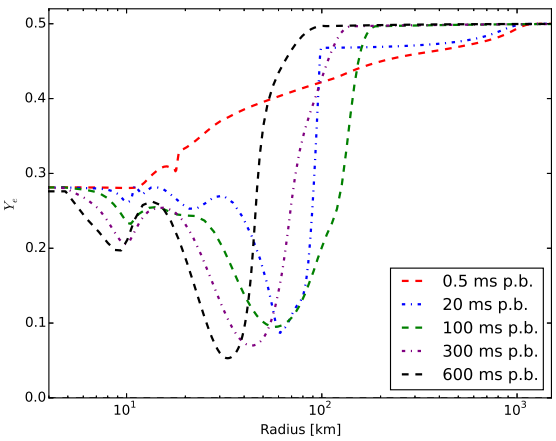

(e) Y_e vs. Radius

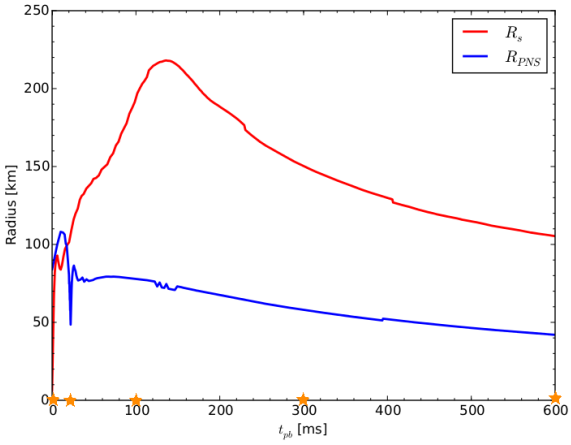

(f) Shock Radius & PNS Surface vs. Time (Post-Bounce)

Figure 11: Hydrodynamics Profiles from Agile-IDSA

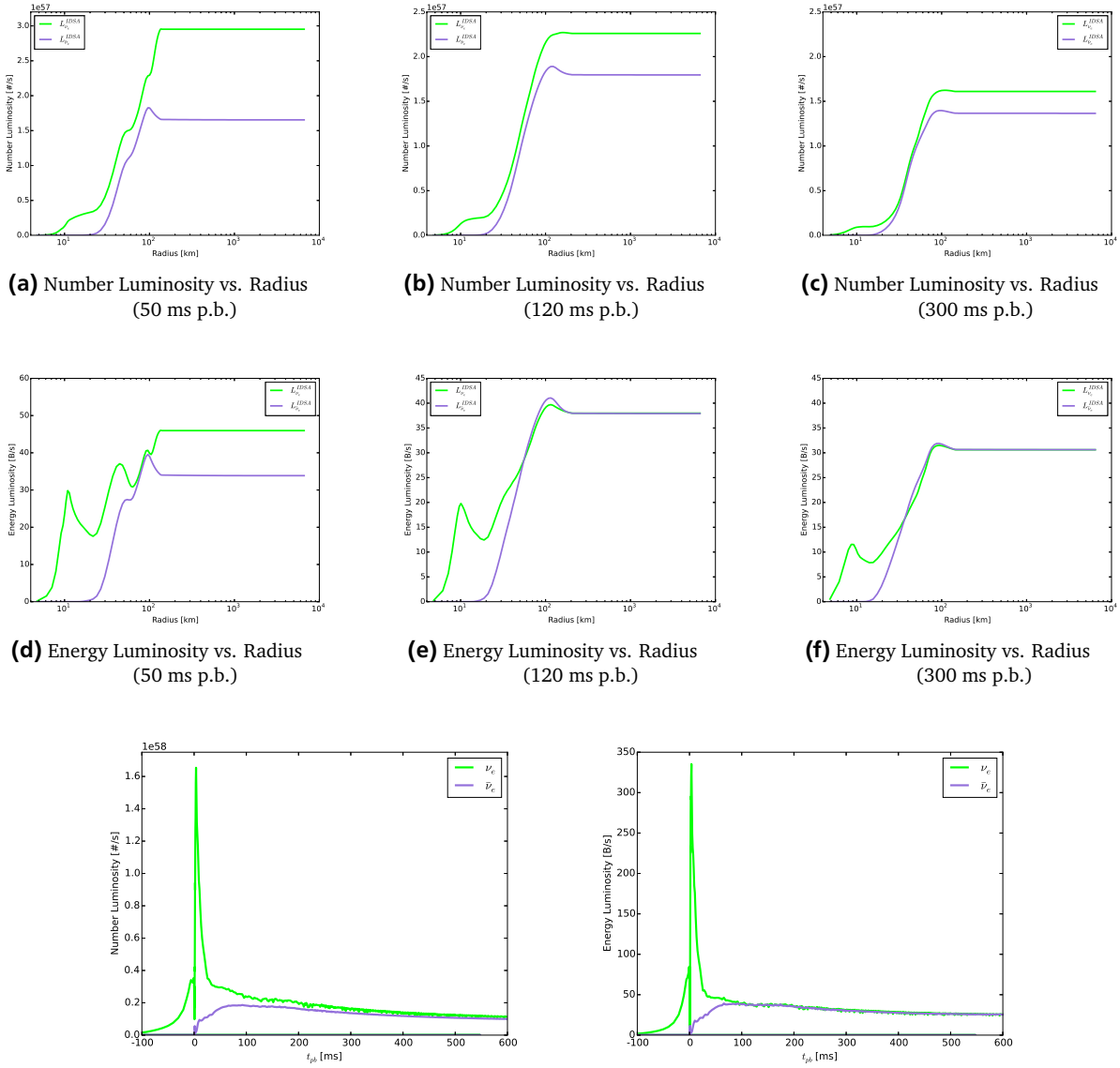

(a) Number Luminosity vs. Radius (50 ms p.b.)

(b) Number Luminosity vs. Radius (120 ms p.b.)

(c) Number Luminosity vs. Radius (300 ms p.b.)

(d) Energy Luminosity vs. Radius (50 ms p.b.)

(e) Energy Luminosity vs. Radius (120 ms p.b.)

(f) Energy Luminosity vs. Radius (300 ms p.b.)

(g) Number Luminosity vs. Time

(h) Energy Luminosity vs. Time

Figure 12: IDSA Profiles from Agile-IDSA

due to the stiffening of the equation of state, which continues to propagate well past 200 km as seen in t_3. Shock stalling is seen becomes evident when one compares the shock fronts at t_3 and t_4. Pulling further back at t_5 proves that the system did not have enough energy to keep the shock expansion going to $r \to \infty$.

The second batch of profiles are provided by IDSA, which provides via the NUPROX module both number and energy luminosity as a function of radius to show incremental absorption and emission of neutrino luminosity throughout the PNS radius. Fortunately for neutrino physics, this is mostly emission, but seeing drops of luminosity can also be indicative of a region of strong re-absorption, such as in the gain region which exists in the domain of $R_\nu < r < R_s$ (and will be discussed later).

Aside from what is infinitesimally produced from shell zone to shell zone, neutrino luminosity is also traditionally characterized by what eventually makes it out of the proto-neutron star atmosphere at $r \to \infty$ at any one instant of time. Figures 14g and 14h show this for the duration of the simulation, with the defining electron neutrino $\boldsymbol{\nu_e}$ burst occurring several milliseconds after bounce (when the shock wave first passes through the neutrinosphere). This is clearly lacking in the anti-neutrino case, as they are not even produced until the post-bounce phase. It is evident that although electron neutrinos dominate in both number and energy luminosity at early times, electron anti-neutrinos $\boldsymbol{\bar{\nu}_e}$ catch up and in "late" evolution ($>$ 200 ms) can be assumed to be approximately equal ($L_{\nu_e} \approx L_{\bar{\nu}_e}$).

2.2.1 Neutrino Energetics

Averaged Quantities: Bracket Notation

The brackets which surround symbols in this work are notation which represent the fact that the code used in this new and independent neutrino transport analysis indeed makes use of quantities which are **grey** and not **spectral**. In IDSA, quantities such as neutrino opacity κ_ν, optical depth τ_ν, mean free path λ_ν, distribution function f_ν, and number/energy luminosities L_ν^N and L_ν are given as functions of energy (e.g. $f_\nu = f_\nu(\epsilon_\nu)$) and are thus treated spectrally, dividing their contributions into pre-determined energy bins. These are technically more accurate, but require more computational power and memory, which could be utilized for other subroutines and analysis. For studies which are only interested in general neutrino characteristics, a grey approach can be quite sufficient.

An example of an averaged quantity used in this study is the **energy-averaged** neutrino cross-section $\langle\sigma_\nu\rangle$:

$$\left.\langle\sigma_{\nu\ell}\rangle \equiv \frac{\int_0^{+\infty} d\epsilon\cdot\epsilon^2\cdot\sigma_{\nu\ell}(\epsilon)\cdot f_{FD}(\epsilon)}{\int_0^{+\infty} d\epsilon\cdot\epsilon^2\cdot f_{FD}(\epsilon)}\right\} \quad \text{where } \sigma_{\nu\ell}(\epsilon)\propto\epsilon_\nu^2$$

Relating the general neutrino cross-section to the baryonic environment around it with ρ, m_b and Y_ℓ with the opacity κ_ν, where $\kappa_{\nu\ell}$ is the opacity due to interaction of ν with particle ℓ and Y_ℓ is the abundance of particle ℓ:

$$\langle\kappa_{\nu\ell}\rangle \equiv \frac{\langle\sigma_{\nu\ell}\rangle\cdot\rho\cdot Y_\ell}{m_b}$$

where $f_{FD}(\epsilon) = \{1+\exp\beta(\epsilon-\mu_\nu)\}^{-1}$ is the Fermi-Dirac distribution and $\beta = 1/T$ is the inverse temperature (expressed in MeV). It is well established that the interaction probability of a neutrino incident upon a neutron (for example) is dependent on the energy of the incident neutrino (From $\sigma_\nu \propto \epsilon_\nu^2$: see Section 2.2.2 and Burrows et al. [2006]). The closed form of this equation is precise, but does not directly answer the question of what the typical or expected magnitude of this value should be in the core-collapse supernova environment. In order to answer this question, it is necessary to determine the magnitude of the mean energy of a neutrino in that particular setting.

Defining Mean Neutrino Energy

The neutrino interaction cross section σ_ν is proportional to the square of the neutrino energy: $\sigma_\nu \propto \epsilon_\nu^2$ [Burrows et al., 2006]. For the sake of simplicity, it is possible to quantify the neutrino particle distribution not as a spectrum of various particles with varying energies, but rather one representative, or **mean energy** $\langle\epsilon_\nu\rangle$. In the following, we will speak of neutrinos in both the streaming and trapped limits. As the words imply, in the streaming limit, neutrinos have a mean free path λ_ν longer than a characteristic length-scale, allowing neutrinos to escape the system with relatively negligible energy and/or momentum loss. In the trapped limit, neutrinos have a mean free path λ_ν much smaller than this characteristic length-scale, causing them to be absorbed and/or scattered. In both regimes, we can assume that in traversing a distance less than its mean free path λ_ν, a neutrino has the same energy it had since its last absorption or scattering interaction, as it could not lose energy or momentum in pure vacuum.

Mean Energy in the Streaming Limit: In order to quantify what could hypothetically be measured by a neutrino detector in space or on the Earth's surface (here disregarding plausible neutrino oscillations in vacuum and in matter for simplicity), we define a mean energy per neutrino $\langle\epsilon_1\rangle$. This quantity can be seen as a time-averaged representation of how much energy has been carried away from the system by neutrinos per a finite and quantified number of said neutrinos. This allows us to build a ratio yielding an effective energy per particle:

$$\boxed{\langle\epsilon_1\rangle = \frac{L_\nu}{L_\nu^N}} \tag{20}$$

Mean Energy in the Trapped Limit: Now, we define a second mean energy $\langle \epsilon_2 \rangle$ which attempts to account for neutrinos which are not yet in the outer, free-streaming region of the PNS environment. In this regime, neutrinos are still readily thermodynamically coupled to matter and are thus in $\boldsymbol{\beta}$ **equilibrium** (in energetic equilibrium with protons, neutrons and electrons), until they themselves eventually diffuse out into less opaque regions. This equilibrium is a simplification which allows the neutrinos to be expressed as a Fermi-Dirac distribution (due to their physical nature as fermions) at a fixed temperature T representative of the surrounding matter and by causality $T = T_\nu$. Keeping the Boltzmann transport equation in mind, the neutrino distribution function $f_\nu(t, r, \mu, \epsilon)$ is dependent on many variables, but in this simplification, we may recover characteristic neutrino behavior without the computational requirements of the BTE.

In seeking to quantify $\langle \epsilon_2 \rangle$, we consider an average energy derived from the neutrino distribution phase space. The time-dependent f_ν is additionally taken to be non-transient, dropping its dependence on t. Even with these assumptions, $f_{FD}(\epsilon)$ is still a function of energy ϵ. Averaging over energy itself allows us to alleviate the quantity of this burden:

$$\langle \epsilon_2 \rangle = \frac{\int d^3\vec{p} \cdot f(t,\vec{x},\vec{p}) \cdot \epsilon}{\int d^3\vec{p} \cdot f(t,\vec{x},\vec{p})} = \frac{\int \left(d\Omega \cdot d\epsilon \cdot \epsilon^2\right) \cdot f(t,\vec{x},\vec{p}) \cdot \epsilon}{\int (d\Omega \cdot d\epsilon \cdot \epsilon^2) \cdot f(t,\vec{x},\vec{p})} \approx \frac{\overbrace{\int d\Omega}^{4\pi} \cdot \int_0^\infty d\epsilon \cdot \epsilon^2 \cdot \epsilon \cdot f_{FD}(\epsilon)}{\underbrace{\int d\Omega}_{4\pi} \cdot \int_0^\infty d\epsilon \cdot \epsilon^2 \cdot f_{FD}(\epsilon)} \tag{21}$$

$$\left.\begin{aligned} \langle \epsilon_2 \rangle \approx \frac{\cancel{4\pi} \cdot \int_0^\infty d\epsilon \cdot \epsilon^3 \cdot f_{FD}(\epsilon)}{\cancel{4\pi} \cdot \int_0^\infty d\epsilon \cdot \epsilon^2 \cdot f_{FD}(\epsilon)} \end{aligned}\right\} \quad \text{where } f_{FD}(\epsilon) = \frac{1}{1 + \exp\left(\frac{\epsilon}{T} - \frac{\mu_\nu}{T}\right)}$$

$$\left.\begin{aligned} \langle \epsilon_2 \rangle \approx \frac{\mathrm{T}^4 \cdot \int_0^\infty dx \, \frac{x^3}{1+\exp(x-\eta_\nu)}}{\mathrm{T}^3 \cdot \int_0^\infty dx \, \frac{x^2}{1+\exp(x-\eta_\nu)}} \end{aligned}\right\} \quad \text{after substitution of } f_{FD}(\epsilon), \ \mathrm{x} = \frac{\epsilon}{T}, \ d\epsilon = T \cdot dx \text{ and } \eta_\nu = \frac{\mu_\nu}{T}$$

$$\boxed{\langle \epsilon_2 \rangle = \mathrm{T} \cdot \frac{\mathcal{F}_3(\eta_\nu)}{\mathcal{F}_2(\eta_\nu)}} \tag{22}$$

where $\mathcal{F}_j(\eta_\nu) = \int_0^\infty dx \, \frac{x^j}{1+\exp(x-\eta)}$ is the Fermi-Dirac integral, j = order of Fermi-Dirac integral, $\mathrm{k_b}$ is the Boltzmann constant, and η_ν the neutrino degeneracy parameter.

Fortunately, this expression is quite simple in showing that mean energy is proportional to temperature to the first order. The only downside to this formalism is that once neutrinos thermally decouple from matter (as shown in the corresponding figures), the neutrino mean-energy as expressed by $\langle \epsilon_2 \rangle$ drops significantly to a level no longer physically representative of neutrino energies (on the order of those observed from SN 1987A, for example). Thus, $\langle \epsilon_2 \rangle$ cannot be true everywhere for all radii and this inconsistency needs to be resolved!

Consolidated Piece-Wise Mean Energy for Both Regions: A mean neutrino energy which can tell the entire story of neutrinos in all radii within the PNS environment is to be expected from any kind of neutrino transport. One limitation of $\langle \epsilon_1 \rangle$ and $\langle \epsilon_2 \rangle$ is that they are derived through two physically distinct concepts. One way to resolve this discrepancy is to consider the energetically decoupled limit (free-streaming) for $r \gtrsim R_\nu^\epsilon$ and the energetically coupled limit (thermal equilibrium) for $r \lesssim R_\nu^\epsilon$, where R_ν^ϵ shall be called the thermal or **energy neutrinosphere**. Somewhere in between is a "fuzzy" point of transition at which the Fermi-Dirac description $\langle \epsilon_2 \rangle$ of the neutrinos is no longer valid, but is simply taken over by the free-streaming luminosity ratio $\langle \epsilon_1 \rangle$. For the sake of notation and completeness, a new, consolidated piece-wise mean energy $\langle \epsilon_3 \rangle$ can be expressed as:

$$\boxed{\langle \epsilon_3 \rangle = \begin{cases} \langle \epsilon_2 \rangle, & \text{for } r \lesssim R_\nu^\epsilon \\ \langle \epsilon_1 \rangle, & \text{for } r \gtrsim R_\nu^\epsilon \end{cases}} \tag{23}$$

2.2.2 Mean Free Path, Optical Depth and Neutrinosphere

What makes neutrinos relevant in the dynamics of an imminent core-collapse supernova, is that baryonic matter is so extremely compact, that neutrinos become relevant and intricate to energy and momentum exchange and transport. Here, we introduce formally the neutrino **mean free path λ_ν** which is defined as:

$$\left.\lambda_\nu = \frac{1}{n\cdot\sigma_\nu} = \frac{1}{\rho\cdot\kappa_\nu^{'}} = \frac{1}{\kappa_\nu}\right\} \quad \begin{array}{c} n = \text{target number density [\#/cm}^3\text{]},\ \sigma_\nu = \text{neutrino cross section [cm}^2\text{]} \\ \rho = \text{target matter density [g/cm}^3\text{]},\ \kappa_\nu^{'} = \text{neutrino opacity [cm}^2\text{/g]} \\ \kappa_\nu = \text{re-scaled neutrino opacity [cm}^{-1}\text{]} \end{array} \tag{24}$$

The mean free path is the average distance which can be travelled by a neutrino before it interacts (via the weak force) with another particle (either via **absorption** mediated by a $W^{\pm}$ boson or **scattering** mediated by a Z boson). As these are two separate physical mechanisms, the total neutrino cross section σ_ν contains two contributions: $\sigma_\nu = \sigma_{\text{abs}} + \sigma_{\text{scat}}$. This is evident in the relation (see Burrows et al. [2006] for a full collection of neutrino-matter cross sections) between the neutrino cross section σ_ν and the neutrino energy ϵ_ν in the case of neutrino absorption on a free neutron ($\nu_e + n \longrightarrow e^- + p$), starting with the commonly used, static reference neutrino cross section σ_o:

$$\sigma_o = \frac{4G_F^2\left(m_e c^2\right)^2}{\pi\left(\hbar c\right)^4} \simeq 1.705\times10^{-44}\text{cm}^2$$

with G_F = the Fermi weak coupling constant ($\simeq 1.436\times10^{-49}$erg/cm^3) and $\hbar$ = reduced Planck's constant ($\hbar = h/2\pi$).

$$\sigma^a_{\nu_e n} = \sigma_o\left(\frac{1+3g_A^2}{4}\right)\left(\frac{\epsilon_{\nu_e}+\Delta_{np}}{m_e c^2}\right)^2\left[1-\left(\frac{m_e c^2}{\epsilon_{\nu_e}+\Delta_{np}}\right)\right]^{1/2} W_M \tag{25}$$

with g_A (~ -1.23) defined as the axial-vector coupling constant, $\Delta_{np} = m_n c^2 - m_p c^2 \sim 1.29$ MeV is the mass-energy difference between a neutron and proton, and W_M is the correction for weak magnetism. For details, see Burrows et al. [2006]. Expressions for the neutrino-nucleon scattering cross sections used in this independent analysis can also be found in the same reference. Matter dependence is expressed in the reciprocal of the mean free path $1/\lambda_\nu$, which can be expressed as the re-scaled neutrino opacity κ_ν [Raffelt, 1996]:

$$\left.\kappa_\nu = \frac{\sigma_\nu\cdot\rho(r)}{m_b}\cdot X_{n/p}(r)\right\} \quad \text{where } X_{n/p} \text{ is the abundance of the target species} \tag{26}$$

In the core-collapse mechanism, neutrinos begin to become very relevant in the energy dynamic of the system. As matter compresses and electron capture in the iron-core continues, density rises, and initially due to scattering off infalling heavy nuclei, neutrino opacity increases. At one point during the collapse itself, density surpasses $\rho_{\text{tr}} > 3\times10^{12}$ g/cm^3, initiating statistical **neutrino trapping**. This creates the beginnings of a region where neutrinos trying to escape the proto-neutron star have a diffusion timescale larger than the timescale of collapse [4]($t_{\text{diff}} > t_{\text{collapse}}$). The neutrino mean free path λ_ν then tends to the same order of magnitude as the radius of the proto-neutron star, and deep inside of the star, will continue to become smaller until λ_ν becomes a value on the order of mere centimeters or less. Table 2 summarizes all the potential weak force mediated interactions which can affect the energetics/momenta of particles in a supernova in its various stages of evolution.

Choice of Mean Free Path λ_ν: As an energy-dependent or *spectral* output quantity, λ_ν is a quantity dependent on both the radius r of the PNS and the energy of the neutrinos of interest, yielding a functional form of $\lambda = \lambda(r, \epsilon_\nu)$. Furthermore, λ_ν exists for both ν_e and $\bar{\nu}_e$, notated as λ_{ν_e} and $\lambda_{\bar{\nu}_e}$ respectively. The variability in λ_ν in radius is due to the matter density ρ of the medium, through which it must propagate (recalling Equation 24).

As Equation 29 refers to a one-dimensional optical depth, it is crucial that it uses a one-dimensional mean free path. By considering an energy-representative, **mean energy**, $\langle\epsilon_\nu\rangle$ it is possible to recover $\lambda = \lambda_\nu(r)$, without explicit energy dependence. Then, an energy-averaged λ_ν per radial shell zone is recovered. This is essentially the idea behind a *grey* neutrino transport scheme, as opposed to a *spectral* consideration.

Not to be overlooked is the fact that a mean free path represents *all* microphysical neutrino interactions with matter. In calculating this quantity from scratch, a total mean free path must be quantified as a superposition of these various interactions. We define the **transport mean free path** λ_ν^t (also commonly called the "sphere of last scattering") as:

$$\lambda_\nu^t = \frac{1}{\left(\frac{1}{\lambda_\nu^{\text{abs}}} + \frac{1}{\lambda_\nu^{\text{scat}}}\right)} \tag{27}$$

[4] Recall the order of magnitude calculation of the collapse time from Section 1.2.3.

Alternatively, if one wishes to emphasize thermalization by absorption, one may define and use the **effective mean free path** λ_ν^ϵ using an absorption-biased geometric mean:

$$\lambda_\nu^\epsilon = \frac{1}{\sqrt{\frac{1}{\lambda_\nu^{\text{abs}}} \cdot \left(\frac{1}{\lambda_\nu^{\text{abs}}} + \frac{1}{\lambda_\nu^{\text{scat}}}\right)}} \tag{28}$$

Determination of Optical Depth: Aside from characterizing the energy of neutrinos, it is also of interest to define how "freely" they move through a medium, in a global way. The **optical depth** τ_ν is an invaluable quantity in studying the global, collective transparency of a medium to neutrinos and how readily they are able to move about and diffuse through that medium. The optical depth is defined as:

$$\tau_\nu(r) = \int_r^\infty \frac{1}{\lambda_\nu(r')}\, dr' = \int_r^\infty \kappa_\nu(r')\, dr' \tag{29}$$

where λ_ν(r) in this context is the *local* mean free path of neutrinos, corresponding to a specific, *local* radius r. The optical depth τ_ν is a *global* quantity, aggregately accounting for the 1D integral path of neutrinos (from a selected $r \to \infty$). As τ_ν is constructed from contributions of λ_ν, it is instructive to consider which form of the mean free path is best to use in an application.

The usefulness of the optical depth is well appreciated in the field of radiation transfer and hydrodynamics, as it represents a global interaction probability of a particle within an environment. Large values of optical depth ($\tau_\nu \gg 1$) indicate regions strongly opaque to neutrino diffusion and small values ($\tau_\nu \ll 1$) indicate regions with little resistance to neutrino diffusion (i.e. free-streaming). The calculation of this quantity given values for λ_ν should then be possible. The discretization of Equation 29 may be performed using various computational algorithms of differing accuracy and sources of error. This implies that the computational estimation of the optical depth is not perfect, but indeed an approximation. As an example, the equation can be discretized using a mid-point integration scheme (for example) as follows:

$$\tau_\nu(r) = \int_r^\infty \frac{1}{\lambda_\nu(r')}\, dr' \quad \to \quad \tau_\nu(r) \approx \sum_{i=1}^{nr-1} \frac{1}{\lambda_\nu(r_i)} \Delta r_i \tag{30}$$

where $\Delta r_i = \frac{r_{i+1} - r_i}{2}$, $nr =$ total number of shell zones, and $\tau_\nu(nr) = 10^{-5}$, as a boundary condition (BC). This particular choice of BC is valid to several orders of magnitude, as the optical depth will tend to a negligible, near-zero value at R_∞.

Neutrinospheres R_ν:

Following the analog of the photosphere as the point where photons freely stream out of a star, neutrinos have a corresponding neutrinosphere. Given the transport mean free path λ_ν^t, the "sphere of last scattering" or **transport neutrinosphere** R_ν^t may be calculated with:

$$\tau_\nu\left(R_\nu^t\right) = \int_{R_\nu^t}^\infty \frac{1}{\lambda_\nu^t(r)}\, dr = {}^2/_3 \tag{31}$$

Conversely, given the effective mean free path λ_ν^ϵ, the energy or **effective neutrinosphere** R_ν^ϵ may be calculated with:

$$\tau_\nu\left(R_\nu^\epsilon\right) = \int_{R_\nu^\epsilon}^\infty \frac{1}{\lambda_\nu^\epsilon(r)}\, dr = {}^2/_3 \tag{32}$$

References hereafter to neutrinospheres will refer to the effective neutrinoshere unless otherwise stated. The opacity κ_ν, optical depth τ_ν and neutrinosphere R_ν quantities are calculated in our neutrino transport analysis with the help of a Fortran subroutine originally written by Hannah Yasin at TU Darmstadt [Yasin, 2013], based on Keil and Janka [1995]. This program was subsequently extensively revised and functionally extended, culminating in the results which appear in Section 3. This theoretical model for the calculation of neutrino opacities and optical depths was extended to estimate heating and cooling due to neutrinos following Janka [2001], as will be introduced next.

2.2.3 Neutrino Cooling and Heating in the Gain Region

Once neutrinospheres for $\boldsymbol{\nu_e}$ and $\bar{\boldsymbol{\nu}}_{\boldsymbol{e}}$ are established, it is critical to assess what the first "free" neutrinos do once they have escaped the diffusive region. For an outside observer, the core within the neutrinosphere effectively serves as a blackbox for neutrino luminosity. Indeed, to a first approximation, it is reasonable to assume that neutrinos in thermal equilibrium with matter will keep that temperature soon after decoupling, and this can be modelled using the Fermi-Dirac distribution $f_\nu^{FD}(\mu_\nu, \epsilon_\nu) = \{\exp[\beta\,(\epsilon_\nu - \mu_\nu]) + 1\}^{-1}$ for neutrinos. Any neutrino number luminosity L_ν^N or energy luminosity L_ν may then be modelled assuming the central object within the neutrinosphere is a Fermi blackbody.

After the neutrino Fermi-Dirac blackbody is established as a source of neutrino luminosity at the boundary condition, what happens then? Indeed, these neutrinos will propagate radially outwards, but will not exit the proto-neutron star environment without interference. The optical depth τ_ν being still on the order of unity implies that neutrinos still have some appreciable probability of interaction. The physical picture past R_ν is that about 10% of the neutrinos released from this point[5] will not escape past the shock radius R_s, but will instead interact, and potentially interact with free nucleons specifically. As they are no longer contained, neutrinos make an effort to diffuse away. This area is known as the **cooling region**, dominated by neutrino emission or *cooling*. The reader has to keep in mind the "fuzziness" of the *grey* definition of the neutrinosphere and the real, physical repercussions of neutrinos having an energy spectrum. Based on the definition of Equations 31 and 32, this leads to $R_\nu = R_\nu(E)$, which we have avoided by just considering a mean energy $\langle\epsilon_\nu\rangle$ and thus a grey value for τ_ν for each neutrino species. As for cooling via emission itself, per the convention used in Janka [2001], the energy loss per unit volume due to neutrino cooling may be denoted by Q_ν^- (with units $\mathrm{erg}\cdot\mathrm{s}^{-1}\cdot\mathrm{cm}^{-3}$), perpetuated through the following reactions:

$$\mathrm{e}^- + \mathrm{p} \longrightarrow \mathrm{n} + \boldsymbol{\nu_e}$$
$$\mathrm{e}^+ + \mathrm{n} \longrightarrow \mathrm{p} + \bar{\boldsymbol{\nu}}_{\boldsymbol{e}}$$

As the shock wave continues to travel outwards (as depicted in Figure 8), free protons and neutrons are left behind in its wake of nuclei dissociation. These are then seen as "fresh targets" for neutrinos trying to make their way out of the PNS atmosphere, yet still have an appreciable mean free path (as corroborated by Figure 19) and thus are absorbed by nucleons. This area is the **gain region**, which is dominated by neutrino absorption.

In reality, these regions are not clear-cut and both neutrino emission and absorption take place in the entirety of the domain of $R_\nu < r < R_s$. Past the cooling region is a characteristic point of transition known as the **gain radius** R_g (as illustrated in Figure 8), where neutrino heating (by neutrino absorption on free nucleons) catches up with neutrino cooling, represented as an energetic gain per unit volume by Q_ν^+ (with units $\mathrm{erg}\cdot\mathrm{s}^{-1}\cdot\mathrm{cm}^{-3}$). Thus, for $r > R_g$: $Q_\nu^+ > Q_\nu^-$ and for $r < R_g$: $Q_\nu^- > Q_\nu^+$. Neutrino absorption (by neutrino luminosity from cooling in the first place) proceeds through the following reactions:

$$\boldsymbol{\nu_e} + \mathrm{n} \longrightarrow \mathrm{p} + \mathrm{e}^-$$
$$\bar{\boldsymbol{\nu}}_{\boldsymbol{e}} + \mathrm{p} \longrightarrow \mathrm{n} + \mathrm{e}^+$$

It should be noted that the aforementioned processes are just **inverses** of each other and would be in equilibrium if conditions were apt (under β equilibrium, for example). This assumption is not valid for $R_\nu < r < R_s$, as strong gradients of density, temperature, and electron fraction make equilibrium impossible. It has been shown in various studies and simulations (Bethe and Wilson [1985], Bethe et al. [1987], Janka and Mueller [1996], Couch and Ott [2013], for example) that these gradients in the gain region drive many hydrodynamic and thermally convective instabilities and non-linear, transient dynamical processes which make the energy exchange mechanism more efficient.

In an effort to qualitatively describe the resulting behavior of the gain region (at least for the effects due to neutrinos), Janka [2001] shows it is possible to estimate cooling based solely on variables such as density ρ, temperature T and electron fraction Y_e. Neutrino heating itself is dependent on the neutrino luminosity L_ν, the square of the neutrino mean energy $\langle\epsilon_\nu^2\rangle$, and flux factor μ_ν. The analytic forms of Q_ν^- and Q_ν^+ (based on Janka [2001]) are as follows:

[5] The reality is that neutrinos of different energy will have different neutrinospheres and so what one neutrino may already consider the free-streaming region, may be considered still to be the diffusion region for another.

$$Q^{+}_{\nu_e} = \frac{3\alpha^2+1}{4}\cdot\frac{\sigma_o\langle\epsilon^2_{\nu_e}\rangle}{(m_e c^2)^2}\cdot\frac{\rho}{m_b}\cdot\frac{L_{\nu_e}}{4\pi r^2\langle\mu_\nu\rangle}\cdot Y_n \quad\Longrightarrow\quad \text{Heating: } \boldsymbol{\nu_e} + \text{n} \longrightarrow \text{p} + \text{e}^- \tag{33}$$

$$Q^{+}_{\bar{\nu}_e} = \frac{3\alpha^2+1}{4}\cdot\frac{\sigma_o\langle\epsilon^2_{\bar{\nu}_e}\rangle}{(m_e c^2)^2}\cdot\frac{\rho}{m_b}\cdot\frac{L_{\bar{\nu}_e}}{4\pi r^2\langle\mu_\nu\rangle}\cdot Y_p \quad\Longrightarrow\quad \text{Heating: } \bar{\boldsymbol{\nu}}_{\boldsymbol{e}} + \text{p} \longrightarrow \text{n} + \text{e}^+ \tag{34}$$

$$Q^{-}_{\nu_e} = \left(3\alpha^2+1\right)\cdot\frac{\pi\sigma_o c\,(kT)^6}{(hc)^3\,(m_e c^2)^2}\cdot\frac{\rho}{m_b}\cdot Y_p\cdot\mathcal{F}_5(\eta_e) \quad\Longrightarrow\quad \text{Cooling: } \text{e}^- + \text{p} \longrightarrow \text{n} + \boldsymbol{\nu_e} \tag{35}$$

$$Q^{-}_{\bar{\nu}_e} = \left(3\alpha^2+1\right)\cdot\frac{\pi\sigma_o c\,(kT)^6}{(hc)^3\,(m_e c^2)^2}\,\frac{\rho}{m_b}\cdot Y_n\cdot\mathcal{F}_5(-\eta_e) \quad\Longrightarrow\quad \text{Cooling: } \text{e}^+ + \text{n} \longrightarrow \text{p} + \bar{\boldsymbol{\nu}}_{\boldsymbol{e}} \tag{36}$$

where $\mathcal{F}_j(\eta)$ denotes the Fermi-Dirac integral function introduced in Section 2.2.1. The total contribution from both species gives us what one expects:

$$\begin{aligned} Q^{+}_{\nu} &= Q^{+}_{\nu_e} + Q^{+}_{\bar{\nu}_e} \\ Q^{-}_{\nu} &= Q^{-}_{\nu_e} + Q^{-}_{\bar{\nu}_e} \end{aligned} \tag{37}$$

The electron degeneracy parameter (as seen in the expressions for neutrino cooling) is defined as $\eta_e = \mu_e/T$, where μ_e is the electron chemical potential (also obtainable from the EOS) and T is the matter temperature. The positron degeneracy parameter is assumed to be the inverse sign of the electron degeneracy parameter: $\eta_{e^-} = -\eta_{e^+} \equiv \eta_e$. An additional assumption in the analysis is that the mean square of the neutrino energy is approximated using the neutrino temperature profile T_ν at $\eta_\nu = 0$, as is done in Janka [2001]:

$$\langle\epsilon^2_{\nu_i}\rangle = \int_0^{+\infty} d\epsilon_\nu \cdot \int_{-1}^{+1} d\mu_\nu\,\epsilon^5_\nu f_{\nu_i} \left(\int_0^{+\infty} d\epsilon_\nu \cdot \int_{-1}^{+1} d\mu_\nu\,\epsilon^3_\nu f_{\nu_i} \right)^{-1} \simeq T^2_{\nu_i}\cdot\frac{\mathcal{F}_5(0)}{\mathcal{F}_3(0)} \approx 20.83_{\ldots}\cdot T^2_{\nu_i}$$

As the units of Q^+_ν and Q^-_ν are expressed dependent on spatial dimension, it is sometimes of interest to consider a heating and cooling rate which considers the amount of heating or cooling per gram of matter, known as the **specific energy rate**:

$$\left.\begin{aligned} q^+_\nu &= \frac{Q^+_\nu}{\rho} \\ q^-_\nu &= \frac{Q^-_\nu}{\rho} \end{aligned}\right\} \quad \text{with dimensions } \left[\frac{\text{erg}}{\text{s}\cdot\text{g}}\right] \tag{38}$$

2.2.4 Macroscopic Effects: Black-Body Luminosity & the Fermi-Dirac Lightbulb

Now that we know that the competition of absorption, emission, and scattering interactions with matter in the gain region drives neutrino heating and cooling, we need a source of neutrinos to escape their respective neutrinospheres to drive the interactions in the first place. The **black-body luminosity** is a useful construction in the field of radiation hydrodynamics and energy transfer that enables us to parametrize a first-order approximation of particle number and energy outflow given a temperature. Even if an object cannot be purely described as a perfectly emissive black-body, it is instructive to consider it as a rough, first approximation. For example, in studies of stellar structure and evolution, one may use the Stefan-Boltzmann Law to relate photonic luminosity L_γ to the effective temperature T_e for a star with (photospheric) radius R using the Stefan-Boltzmann constant $\sigma_{\text{SB}} = 2\,\pi^5\,k_B^4/15\,c^2\,h^3$:

$$L_\gamma = 4\,\pi\,R^2\cdot\overbrace{\sigma_{\text{SB}}\cdot T_e^4}^{\text{energy flux } F_\gamma}$$

In the case of neutrinos, it is known that in the trapping region ($\rho \gtrsim 10^{11}$ g/cm^3), neutrinos are in thermal equilibrium with the surrounding matter. This implies that neutrinos are sharing their energy with surrounding particles to sustain β equilibrium. Where this ends is the particular radius R^ϵ_ν which was introduced in our previous discussion. After neutrinos

decouple thermally from baryonic matter past R^{ϵ}_{ν}, they have a different temperature profile $T = T_{\nu}$ and must be treated as an independent quantity. In this section, we focus the attention of the reader to the estimation of the black-body luminosity at R^{ϵ}_{ν}.

As described in Janka [1995], the neutrino spectra that are produced in the post-bounce PNS environment can be estimated to have originated from a particular temperature within the proto-neutron star. Each part of this spectrum is a superposition of contributions from all the various thermal decoupling, energy neutrinospheres $R^{\epsilon}_{\nu} = R^{\epsilon}_{\nu}(E)$. For the application presented in the following, the dynamics inside of the energetic decoupling sphere is irrelevant, and we assume one fixed radius in time (the grey, energy neutrinosphere for both $\boldsymbol{\nu_e}$ and $\boldsymbol{\bar{\nu}_e}$) to represent this boundary condition. Following Janka [1995], the neutrino number flux given a Fermi-Dirac black-body is given by:

$$\left.\begin{aligned} F^{N}_{\nu} = \vec{f} \cdot c \cdot n_{\nu} = \frac{1}{4} \cdot c \cdot n_{\nu} \end{aligned}\right\} \quad \text{where } n_{\nu} = \text{neutrino } \textbf{number} \text{ density} \tag{39}$$

and for the neutrino energy flux:

$$\left.\begin{aligned} F_{\nu} = \vec{f} \cdot c \cdot u_{\nu} = \frac{1}{4} \cdot c \cdot u_{\nu} \end{aligned}\right\} \quad \text{where } u_{\nu} = \text{neutrino } \textbf{energy} \text{ density} \tag{40}$$

where the vacuum approximation[6] $\left(\vec{f} = 1/4\right)$ for the flux factor $\vec{f}$ has been made.

Following the analytic formalism of 2.2.1, the neutrino number density n_{ν} is explicitly derived as:

$$\left.\begin{aligned} n_{\nu} = \frac{4\pi}{(hc)^3} \cdot \int_0^{+\infty} \frac{\epsilon^2 \cdot d\epsilon}{1 + \exp\left(\frac{\epsilon}{T_{\nu}} - \eta_{\nu}\right)} = \frac{4\pi}{(hc)^3} \cdot (k_B\, T_{\nu})^3 \cdot \mathcal{F}_2(\eta_{\nu}) \end{aligned}\right\} \quad \text{with dimensions } [\#/\text{cm}^3] \tag{41}$$

and the neutrino energy density u_{ν} is found with:

$$\left.\begin{aligned} u_{\nu} = \frac{4\pi}{(hc)^3} \cdot \int_0^{+\infty} \frac{\epsilon^3 \cdot d\epsilon}{1 + \exp\left(\frac{\epsilon}{T_{\nu}} - \eta_{\nu}\right)} = \frac{4\pi}{(hc)^3} \cdot (k_B\, T_{\nu})^4 \cdot \mathcal{F}_3(\eta_{\nu}) \end{aligned}\right\} \quad \text{with dimensions } [\text{MeV}/\text{cm}^3] \tag{42}$$

Substituting these quantities into the equations above gives us both the neutrino number and energy flux:

$$\implies \quad F^{N}_{\nu} = \frac{1}{4} \cdot c \cdot \overbrace{\left[\frac{4\pi}{(hc)^3} \cdot (k_B\, T_{\nu})^3 \cdot \mathcal{F}_2(\eta_{\nu})\right]}^{\text{Equation 41}} = \pi \cdot \frac{(k_B\, T_{\nu})^3}{c^2 \cdot h^3} \cdot \mathcal{F}_2(\eta_{\nu}) \tag{43}$$

$$\implies \quad F_{\nu} = \frac{1}{4} \cdot c \cdot \overbrace{\left[\frac{4\pi}{(hc)^3} \cdot (k_B\, T_{\nu})^4 \cdot \mathcal{F}_3(\eta_{\nu})\right]}^{\text{Equation 42}} = \pi \cdot \frac{(k_B\, T_{\nu})^4}{c^2 \cdot h^3} \cdot \mathcal{F}_3(\eta_{\nu}) \tag{44}$$

where h is Planck's constant, c the speed of light, η_{ν} the neutrino degeneracy parameter, $\mathcal{F}_3(\eta_{\nu})$ the third order Fermi-Dirac integral function, and $\mathcal{F}_2(\eta_{\nu})$ for the second order. Unlike the reference, we do not outright assume a zero chemical potential for the neutrino degeneracy parameter η_{ν}, thus $(\mu_{\nu} \neq 0)$. The equations for n_{ν} and u_{ν} should be reminiscent of those performed in Section 2.2.1. Finally, recalling what we know about the relation of luminosity to flux (from Equation 1) and substituting:

$$L^{N,FD}_{\nu} = 4\pi \cdot \left(R^{\epsilon}_{\nu}\right)^2 \cdot F^{N}_{\nu} = 4\pi \cdot \left(R^{\epsilon}_{\nu}\right)^2 \cdot \overbrace{\left[\pi \cdot \frac{(k_B\, T_{\nu})^3}{c^2 \cdot h^3} \cdot \mathcal{F}_2(\eta_{\nu})\right]}^{\text{Equation 43}} = \frac{4\pi^2}{c^2 \cdot h^3} \cdot \left(R^{\epsilon}_{\nu}\right)^2 \cdot (k_B\, T_{\nu})^3 \cdot \mathcal{F}_2(\eta_{\nu}) \tag{45}$$

$$L^{FD}_{\nu} = 4\pi \cdot \left(R^{\epsilon}_{\nu}\right)^2 \cdot F_{\nu} = 4\pi \cdot \left(R^{\epsilon}_{\nu}\right)^2 \cdot \overbrace{\left[\pi \cdot \frac{(k_B\, T_{\nu})^4}{c^2 \cdot h^3} \cdot \mathcal{F}_3(\eta_{\nu})\right]}^{\text{Equation 44}} = \frac{4\pi^2}{c^2 \cdot h^3} \cdot \left(R^{\epsilon}_{\nu}\right)^2 \cdot (k_B\, T_{\nu})^4 \cdot \mathcal{F}_3(\eta_{\nu}) \tag{46}$$

where the latter terms are free variables for the determination of L_{ν}. Generally speaking, the degeneracy parameter of a degenerate particle species x is defined as $\eta_x = \mu_x / T$. The assumption of degeneracy plays an important role in deciding whether the system may energetically accommodate a particle. As the value of the Fermi-Dirac integral function $\mathcal{F}_j(\eta_{\nu})$ for neutrinos can vary several orders of magnitude based on the value of η_{ν} alone, it is critical to make the right choice. Unfortunately, making such a choice is not trivial. Analysis dedicated to constraining these degrees of freedom follows in the corresponding Results section.

[6] see Janka [1995]

2.3 Neutrino Optical Depth and Luminosity Estimation Program (NODALEP)

2.3.1 Number Luminosity Calculation Scheme

The neutrino number luminosity (in units of #/s) outside of the neutrinosphere[7] r_o at a radial position r is estimated using the following equation:

$$L_\nu^N(r) = L_\nu^N(r_o) \cdot \exp\left\{-\int_{r_o}^{r} dr' \frac{\langle \kappa_{\text{abs}} \rangle}{\langle \mu_\nu \rangle}\right\} + \int_{r_o}^{r} dr' \cdot 4\pi(r')^2 \cdot R_\nu^- \cdot \exp\left\{-\int_{r'}^{r} dr'' \frac{\langle \kappa_{\text{abs}} \rangle}{\langle \mu_\nu \rangle}\right\} \tag{47}$$

where $\langle \kappa_{\text{abs}} \rangle$ is the energy-averaged absorption opacity, $\langle \mu_\nu \rangle$ is the flavor-averaged flux factor, and R_ν^- is the **neutrino number emission rate** (in units of $[\# \cdot s^{-1} \cdot \text{cm}^{-3}]$)

This equation may be decomposed into two parts, separated by the plus sign. The first may be seen as a sort of number luminosity Fermi-Dirac blackbody "light bulb" condition, where r_o represents the radial location of the neutrinosphere, or where neutrinos are thereafter free to stream out into regions of optical depth $\tau \ll 1$. The matter confined within the radius r_o is statistically considered to be trapped and is thusly represented as having a mean energy comparable to the temperature distribution (remembering $\langle \epsilon_\nu \rangle \approx \mathcal{F}_3(\eta_\nu)/\mathcal{F}_2(\eta_\nu) \cdot T$). Given Equation 47, we assume the characteristics of the proto-neutron star within r_o are unknown, and thus a blackbox. **This luminosity calculation scheme can thus only estimate luminosities outside of** r_o. In spite of this constraint, it must be repeated that the neutrinosphere is not a rigidly defined quantity in neutrino transport theory and thus its very definition as a single radial point (especially for all neutrino energies) serves as a known and acceptable source of error.

At an arbitrary radius r (greater than r_o), the neutrino number luminosity $L_\nu^N(r)$ is a superposition of that which comes from the neutrino number "light bulb" blackbody (at r_o), and that which is emitted from neutrino emission processes thereafter. Both phenomena are manifest in Equation 47:

- The first term carries an $\exp\{-\int \dots\}$ term which represents how much of that original light bulb number luminosity gets dampened or attenuated (from successive re-absorption, proportional to the strength of $\langle \kappa_{\text{abs}} \rangle$) from the still dense matter. The integration range in the $\exp\{-\int \dots\}$ term represents the radial range which is being considered in a calculation.

$$= \overbrace{L_\nu^N(r_o)}^{\text{boundary condition (BC)}} \cdot \underbrace{\exp\left\{-\int_{r_o}^{r} dr' \frac{\langle \kappa_{\text{abs}} \rangle}{\langle \mu_\nu \rangle}\right\}}_{\text{BC attentuation}} + \cdots$$

- The second term represents the cumulative cooling (and thus increase of neutrino number luminosity) from all radial shells leading up to the radial point being considered at r. Since neutrinos are being emitted at every shell zone (here r') prior to r, each successive contribution must also account for its own re-absorption in the PNS material leading up to that same point r. Neutrino number emission is represented by R_ν^-, which in this work has units of $\left[\#/\left(\text{s} \cdot \text{cm}^3\right)\right]$.

$$\cdots + \int_{r_o}^{r} dr' \cdot \overbrace{4\pi(r')^2 \cdot R_\nu^-}^{\nu \text{ emission flux}} \cdot \underbrace{\exp\left\{-\int_{r'}^{r} dr'' \frac{\langle \kappa_{\text{abs}} \rangle}{\langle \mu_\nu \rangle}\right\}}_{\text{re-absorption of } \nu \text{ emission flux}}$$

For the ν-sphere we use Equations 31 and 32. See section 2.2.2 for a discussion of transport vs. energy neutrinospheres and their definitions.

[7] the neutrinosphere here is presented as a conceptual construct, regardless of the previously made calculations and assumptions

Determination of Flux Factor $\langle \mu_\nu \rangle$

The flux factor term $\langle \mu_\nu \rangle$ has its origins in the original derivation of the Boltzmann transport equation for the radiation transport of neutrinos in a medium (where it is also commonly denoted by $\vec{f}$). It is also commonly called the "geometrical factor" which determines the direction of neutrino propagation in the PNS environment. As it is an approximate scheme assuming isotropy, the isotropic diffusion source approximation (IDSA) does not directly treat or calculate μ_ν as the full BTE does. In order to replicate the behavior, as μ_ν remains a physically decisive quantity, neutrinos are assumed to be emitted isotropically at their scattering/transport spheres R^t_ν, as shown by Equation 11 in Liebendörfer et al. [2009]. Alternative derivations of this value either empirically or using fits can be found in Janka [1991], Janka and Hillebrandt [1989], and Janka and Hillebrandt [1989].

For the purposes of the code utilized in this work, we applied a fitting scheme similar to the one used by IDSA to set a flux factor which mimics the behavior of a rigorous BTE approach. At or near the scattering neutrinosphere, $\langle \mu_\nu \rangle$ is defined to be $^1/_4$ and approaches a value of unity (~ 1) at the free-streaming limit (as $r \to \infty$). The behavior between these two values has been studied extensively in Janka [1991] and Janka [1995], in which alternate forms for an approximate fit have been suggested.

2.3.2 Energy Luminosity Calculation Scheme

For the calculation of the neutrino energy luminosity L_ν, Equation 20 was used. This implies that in this estimation algorithm, the **energy luminosity may only be computed once the number luminosity is known**. Due to the usage of a relation which only applies for $r > R_\nu$, the estimation of energy luminosity within the neutrinosphere in this fashion will be inaccurate, as we have made the assumption of a Fermi-Dirac blackbody "light bulb" to be a boundary condition at the neutrinosphere.

As we want to use this relation for luminosity estimation for both $\boldsymbol{\nu_e}$ and $\boldsymbol{\bar{\nu}_e}$, it is advisable to consider this assumption valid only when both species are streaming freely. Thus, we claim this assumption valid only outside the most consistently external neutrinosphere $\left(r > R^t_{\nu_e}\right)$:

$$L_\nu(r) = \langle \epsilon_\nu \rangle \cdot L^N_\nu(r) \tag{48}$$

It is evident that $\langle \epsilon_\nu \rangle$ serves as a scalar attenuating factor to L^N_ν. In order to quantify L_ν, one simply needs to determine a value for $\langle \epsilon_\nu \rangle$. The simplest case involves the assumption of neutrino chemical potential being equal to zero ($\eta_\nu = 0$):

$$\langle \epsilon_\nu \rangle = \mathrm{T} \cdot \overbrace{\frac{\mathcal{F}_3(0)}{\mathcal{F}_2(0)}}^{\sim 3.15\ldots} \quad \longrightarrow \quad \langle \epsilon_\nu \rangle \sim \mathrm{T} \times 3.15\ldots$$

The Assumption of Constant Mean-Energy

I make the claim and now apply the caveat that the mean energy *at the transport neutrinosphere* R^t_ν should be used to determine the energy luminosity even far away from the neutrinosphere. This makes the assumption that the neutrino mean energy does **not** change appreciably between the transport neutrinosphere R^t_ν and $r \to \infty$, as though only energy-conserving processes (such as purely elastic scattering) dominated neutrino transport outside of the energy neutrinosphere. This is a physically bold claim, but is valid within a small margin of error.

To account for the margin of error, we recall that neutrinos propagate with various energies (bringing the spectrum into play). Since neutrinos with higher energy are absorbed more readily than less energetic ones (again recalling $\sigma_\nu \propto E^2_\nu$), a sort of spectral "clipping" takes place, thereby shifting the mean energy slightly, as neutrinos travel outside of the gain region, eventually leaving the system at low optical depths ($\tau_\nu \ll 1$).

Thus, for the final form of the neutrino energy luminosity, I claim:

$$L_\nu(r) = \left\{ \langle \epsilon_\nu \rangle \big|_{r=R^t_\nu} \right\} \cdot L^N_\nu(r) \approx \left\{ T(R^t_\nu) \cdot \frac{\mathcal{F}_3(0)}{\mathcal{F}_2(0)} \right\} \cdot L^N_\nu(r)$$

$$\boxed{L_\nu(r) \approx T(R^\epsilon_\nu) \cdot \frac{\mathcal{F}_3(0)}{\mathcal{F}_2(0)} \cdot L^N_\nu(r)} \tag{49}$$

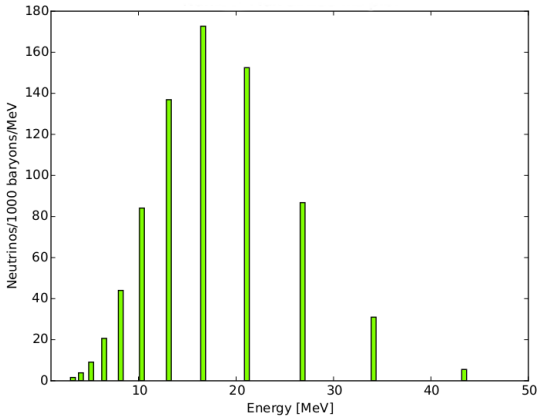

Figure 13: Typical ν Energy Spectrum

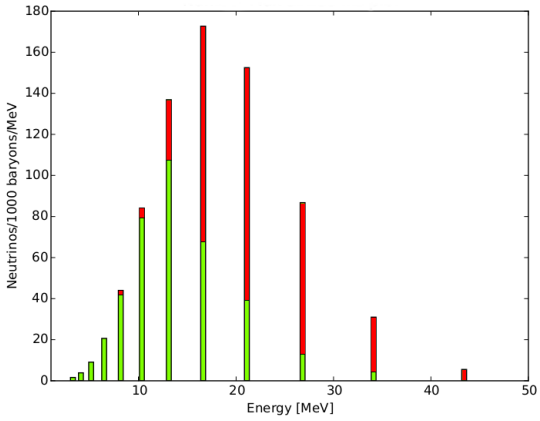

Figure 14: Conceptualization of Theoretical "Clipping": Red denotes biased absorption of higher energies

2.3.3 Change in Energy $\dot{e}$ and Electron Abundance $\dot{Y}_e$ Due to Neutrino Interactions

Eventually, one would like to couple the neutrino transport to a hydrodynamics code, as explained before with Agile-IDSA. To the end, two key quantities have to be calculated: the specific energy rate due to neutrinos $\dot{e}$ and the change in electron abundance $\dot{Y}_e$ due to their interactions with matter. The electron abundance Y_e is a critical quantity in determining the neutron- or proton-richness of stellar matter. During the core-collapse, bounce, and post-bounce phases of a CCSN, matter strongly deleptonizes, losing both neutrinos and electrons acting via the weak force to change protons into neutrons. The lepton number Y_L accounts for changes in both electrons and neutrinos, whereas the electron number Y_e only accounts for changes in electrons. We will concentrate here on the latter quantity.

Defining Electron Abundance Loss and Gain in Time

The foundation of this effect in a computer simulation is based on the following physical neutrino reactions with baryonic matter (in the case of neutrino absorption, without the assumption of processes being equilibriated with their inverse process):

$$e^- + p \longrightarrow n + \boldsymbol{\nu_e} \quad : \quad r^-_{\nu_e} \tag{50a}$$

$$e^+ + n \longrightarrow p + \bar{\boldsymbol{\nu}}_{\boldsymbol{e}} \quad : \quad r^-_{\bar{\nu}_e} \tag{50b}$$

$$n + \boldsymbol{\nu_e} \longrightarrow e^- + p \quad : \quad r^+_{\nu_e} \tag{50c}$$

$$p + \bar{\boldsymbol{\nu}}_{\boldsymbol{e}} \longrightarrow e^+ + n \quad : \quad r^+_{\bar{\nu}_e} \tag{50d}$$

These four exchange reactions are those which are capable of changing the electron abundance Y_e of a closed system on account of neutrinos. For the purposes of this work, each process shall be assigned an associated **specific neutrino number absorption or emission rate** (with units of $[\#/(g \cdot s)]$) indicated by $r^{+/-}_{\nu_e/\bar{\nu}_e}$ (not to be confused with a measure of length or distance). Equations 50b and 50c increase the electron abundance ($Y_e \uparrow$ or $\dot{Y}_e > 0$), whereas Equations 50a and 50d decrease it ($Y_e \downarrow$ or $\dot{Y}_e < 0$). Thus, when considering what the global effect of these four reactions is, one may build an effective $\dot{Y}_e$ (using reaction rates $\lambda_{ab\to cd}$ in the notation of Qian and Woosley [1996]) which counts every $Y_e \uparrow$ and $Y_e \downarrow$ in an automated fashion, and which is simultaneously dimensionally sound:

$$\dot{Y}_e = \frac{\partial Y_e}{\partial t} = \lambda_{e^+ n \to p \bar{\nu}_e} + \lambda_{n \nu_e \to e^- p} - \lambda_{e^- p \to n \nu_e} - \lambda_{p \bar{\nu}_e \to e^+ n} \tag{51}$$

Re-organizing into species-specific contributions and being mindful of dimensions yields:

$$\dot{Y}_e = \frac{\partial Y_e}{\partial t} = \left[\underbrace{\left(-r^-_{\nu_e} + r^+_{\nu_e} \right)}_{\text{electron neutrinos}} + \overbrace{\left(r^-_{\bar{\nu}_e} - r^+_{\bar{\nu}_e} \right)}^{\text{electron anti-neutrinos}} \right] \cdot m_b \tag{52}$$

Fortunately, this quantity may already be calculated within the framework of the NODALEP code through neutrino number luminosity. Using dimensional analysis and what we already know about neutrino number absorption and emission rates (r_ν^+ and r_ν^- respectively, with units of $[\#/(\mathrm{g}\cdot\mathrm{s})]$), it is possible to create luminosity-specific rate equivalence relations which account for local positive or negative contributions to L_ν^N due to $r_{\nu_e/\bar{\nu}_e}^{+/-}$:

$$\begin{aligned}\frac{1}{4\pi r^2\rho}\frac{\partial L_{\nu_e}^N(r)}{\partial r} &= -r_{\nu_e}^+(r)+r_{\nu_e}^-(r)\\ \frac{1}{4\pi r^2\rho}\frac{\partial L_{\bar{\nu}_e}^N(r)}{\partial r} &= -r_{\bar{\nu}_e}^+(r)+r_{\bar{\nu}_e}^-(r)\end{aligned} \tag{53}$$

Dimensionally, it is clear that $\partial L_\nu^N/\partial r$ is not enough to get $\dot{Y}_\mathrm{e}$, as the former has units of $[\#/(\mathrm{s}\cdot\mathrm{cm})]$ and the latter having $[\#/\mathrm{s}]$. The addition of a specific volume term accounting for the target baryon mass solves this problem. Combining the luminosity-specific rate equivalence relations and the derivation for $\dot{Y}_\mathrm{e}$ yields:

$$\boxed{\dot{Y}_\mathrm{e}=\frac{\partial Y_e}{\partial t}=\left[\frac{\partial L_{\bar{\nu}_e}^N}{\partial r}-\frac{\partial L_{\nu_e}^N}{\partial r}\right]\cdot\frac{m_\mathrm{b}}{4\pi r^2\rho}} \tag{54}$$

Defining Energy Loss and Gain in Time

Similiarly, the same analysis may be utilized in the determination of $\dot{e}$, but now for energy loss and gain through cooling and heating, respectively:

$$e^- + p \longrightarrow n + \boldsymbol{\nu_e} \quad : \quad q_{\nu_e}^- \tag{55a}$$
$$e^+ + n \longrightarrow p + \boldsymbol{\bar{\nu}_e} \quad : \quad q_{\bar{\nu}_e}^- \tag{55b}$$
$$n + \boldsymbol{\nu_e} \longrightarrow e^- + p \quad : \quad q_{\nu_e}^+ \tag{55c}$$
$$p + \boldsymbol{\bar{\nu}_e} \longrightarrow e^+ + n \quad : \quad q_{\bar{\nu}_e}^+ \tag{55d}$$

We now define energy loss and gain due to neutrinos in the proto-neutron star environment using specific neutrino energy absorption and emission rates (q_ν^+ and q_ν^- respectively, with units of $[\mathrm{erg}/(\mathrm{g}\cdot\mathrm{s})]$). The rate of energy change within the system due to neutrinos is then the superposition of how much energy is gained through neutrino absorption and how much is lost through neutrino emission (for both ν_e and $\bar{\nu}_e$):

$$\dot{e}=\frac{\partial e}{\partial t}=\left[\underbrace{\left(q_{\nu_e}^+-q_{\nu_e}^-\right)}_{\text{electron neutrinos}}+\overbrace{\left(q_{\bar{\nu}_e}^+-q_{\bar{\nu}_e}^-\right)}^{\text{electron anti-neutrinos}}\right] \tag{56}$$

Recalling the luminosity-specific rate equivalence relations and considering an analogous form:

$$\begin{aligned}\frac{1}{4\pi r^2\rho}\frac{\partial L_{\nu_e}(r)}{\partial r} &= -q_{\nu_e}^+(r)+q_{\nu_e}^-(r)\\ \frac{1}{4\pi r^2\rho}\frac{\partial L_{\bar{\nu}_e}(r)}{\partial r} &= -q_{\bar{\nu}_e}^+(r)+q_{\bar{\nu}_e}^-(r)\end{aligned} \tag{57}$$

Substituting the equivalence relations and $\dot{e}$ yields:

$$\boxed{\dot{e}=\frac{\partial e}{\partial t}=-\left[\frac{\partial L_{\nu_e}}{\partial r}+\frac{\partial L_{\bar{\nu}_e}}{\partial r}\right]\cdot\frac{1}{4\pi r^2\rho}} \tag{58}$$

2.3.4 Behavior Within Neutrinosphere: The Diffusion Regime

Up until now, we had assumed the following in the derivation of $\dot{e}$ and $\dot{Y}_e$:

$$\dot{e} = \begin{cases} 0 & \text{if } r < R^t_{\nu_e} \\ -\left[\dfrac{\partial L_{\nu_e}}{\partial r} + \dfrac{\partial L_{\bar{\nu}_e}}{\partial r}\right] \cdot \dfrac{1}{4\pi r^2 \rho} & \text{if } r > R^t_{\nu_e} \end{cases}$$

$$\dot{Y}_e = \begin{cases} 0 & \text{if } r < R^t_{\nu_e} \\ \left[\dfrac{\partial L^N_{\bar{\nu}_e}}{\partial r} - \dfrac{\partial L^N_{\nu_e}}{\partial r}\right] \cdot \dfrac{m_b}{4\pi r^2 \rho} & \text{if } r > R^t_{\nu_e} \end{cases}$$

To complete the model for the entire radial range, it is necessary to improve our assumption for $r < R_\nu$. Using Rosswog and Liebendörfer [2003] as a reference, trapped neutrinos and anti-neutrinos are modeled as a Fermi gas which diffuse with timescale t_{diff}. Rosswog et al. refer to Ruffert et al. [1996] and Ruffert et al. [1997] to suggest the following form for t_{diff} (using the total mean free path and optical depth, as opposed to the effective values):

$$t_{\text{diff}} = \frac{\alpha \cdot \lambda_\nu \cdot \tau_\nu^2}{c}$$

where α = scalar diffusion parameter and c = speed of light [cm/s].

Following the example set by Rosswog and Liebendörfer [2003], we utilize formulas to derive values (using a subroutine written specifically to allocate, separate and distribute ne energy bins for neutrinos which is also used in IDSA, see Liebendörfer et al. [2009]) for **neutrino number density** and the **neutrino energy density** (defined as n_ν and u_ν respectively), expressed below:

$$\left.\begin{aligned} n_\nu = \frac{4\pi}{(hc)^3} \cdot \int_0^{+\infty} \frac{\epsilon^2 \cdot d\epsilon}{1 + \exp\left(\frac{\epsilon}{T} - \eta_\nu\right)} \quad \xrightarrow{\text{Discretized as}} \quad n_\nu = \frac{4\pi}{(hc)^3} \cdot \sum_{i=1}^{ne} \frac{\epsilon_i^2 \cdot \Delta\epsilon_i}{1 + \exp\left(\frac{\epsilon_i}{T} - \eta_\nu\right)} \end{aligned}\right\} \quad \text{with units of } \left[\#/\text{cm}^3\right]$$

$$\left.\begin{aligned} u_\nu = \frac{4\pi}{(hc)^3} \cdot \int_0^{+\infty} \frac{\epsilon^3 \cdot d\epsilon}{1 + \exp\left(\frac{\epsilon}{T} - \eta_\nu\right)} \quad \xrightarrow{\text{Discretized as}} \quad u_\nu = \frac{4\pi}{(hc)^3} \cdot \sum_{i=1}^{ne} \frac{\epsilon_i^3 \cdot \Delta\epsilon_i}{1 + \exp\left(\frac{\epsilon_i}{T} - \eta_\nu\right)} \end{aligned}\right\} \quad \text{with units of } \left[\text{erg/cm}^3\right]$$

Now, once these quantities are calculated using the assumption of β equilibrium for neutrinos (relating chemical potentials of neighboring protons μ_p, neutrons μ_n, electrons μ_e and matter temperature T with the neutrino degeneracy parameter η_ν), number luminosities coming from within the opaque region may be calculated using n_ν and the same can be done for energy luminosities with u_ν (strictly for $r \leq R^\epsilon_\nu$):

$$\left.\begin{aligned} L^{N,\text{diff}}_\nu(r) = k \cdot \int_0^r 4\pi(r')^2 \cdot \overbrace{\frac{n_\nu(r')}{\langle t_{\text{diff}}\rangle(r')}}^{\text{analog to } R^-_\nu} \cdot dr' \quad \xrightarrow{\text{Discretized as}} \quad L^{N,\text{diff}}_\nu(r) = k \cdot 4\pi \cdot \sum_{i=1}^{r} \overbrace{\frac{n_\nu(r_i)}{\langle t_{\text{diff}}\rangle(r_i)}}^{\text{analog to } R^-_\nu} \cdot r_i^2 \cdot \Delta r_i \end{aligned}\right\} \quad \text{with units of } [\#/s]$$

$$\left.\begin{aligned} L^{\text{diff}}_\nu(r) = k' \cdot \int_0^r 4\pi(r')^2 \cdot \overbrace{\frac{u_\nu(r')}{\langle t_{\text{diff}}\rangle(r')}}^{\text{analog to } Q^-_\nu} \cdot dr' \quad \xrightarrow{\text{Discretized as}} \quad L^{\text{diff}}_\nu(r) = k' \cdot 4\pi \cdot \sum_{i=1}^{r} \overbrace{\frac{u_\nu(r_i)}{\langle t_{\text{diff}}\rangle(r_i)}}^{\text{analog to } Q^-_\nu} \cdot r_i^2 \cdot \Delta r_i \end{aligned}\right\} \quad \text{with units of } [\text{erg}/s]$$

Once these forms have been integrated, they must also have a continuous transition and thus agree with the boundary condition of the Fermi-Dirac blackbody light bulb term at R^ϵ_ν. This is precisely the motivation for a rescaling of the terms with constants of integration k and k', relative to $L^{N,FD}_\nu(R^\epsilon_\nu)$ and $L^{N,FD}_\nu(R^\epsilon_\nu)$ respectively, such that they match at the

boundary. Thus, this effectively is the spreading out or *re-allocation* of the blackbody light bulb's luminosity into radial zones whose total contribution is simply the boundary condition luminosity itself. The forms of k and k' are:

$$k = \frac{L^{N,FD}(R_\nu^\epsilon)}{\int_0^{R_\nu^\epsilon} 4\pi(r')^2 \cdot \frac{n_\nu(r')}{\langle t_{\text{diff}}\rangle(r')} \cdot dr'} \qquad k' = \frac{L^{FD}(R_\nu^\epsilon)}{\int_0^{R_\nu^\epsilon} 4\pi(r')^2 \cdot \frac{u_\nu(r')}{\langle t_{\text{diff}}\rangle(r')} \cdot dr'}$$

The forms of these radial integrals should remind the reader of the cooling term (second term) in Equation 47. They are indeed analogous to $R_\nu^\pm$ and $Q_\nu^\pm$, but lack the same $\exp\left\{-\int \ldots\right\}$ terms which follow. This is simply due to the fact that neutrino-matter interactions here are in β equilibrium and no noteworthy energy gain or loss exists in this regime. Additionally, the notation $\langle t_{\text{diff}}\rangle$ implies that the quantities λ_ν and τ_ν used within the calculation of t_{diff} were simply the energy-averaged quantities previously introduced in calculations of mean free path and optical depth.

The inclusion of these sources of neutrino luminosity are intended to effectively "spread" out the luminosity at the Fermi-Dirac light bulb blackbody condition, loosening the ambiguous title of "blackbox" for the blackbody luminosity. The integrated values of $L_\nu^{N,\text{diff}}$ and L_ν^{diff} will add up to some arbitrary value at any given $r < R_{\bar{\nu}_e}^\epsilon$, but must agree with the number and energy luminosity values once they reach the light bulb boundary condition. Using a convenient normalization, it is possible to scale all the calculated values for $L_\nu^{N,\text{diff}}$ and L_ν^{diff} at each radius such that there is a smooth transition between the diffusion regime and the boundary condition:

$$\dot{e} = \begin{cases} -\left[\frac{\partial L_{\nu_e}^{\text{diff}}}{\partial r} + \frac{\partial L_{\bar{\nu}_e}^{\text{diff}}}{\partial r}\right] \cdot \frac{1}{4\pi r^2 \rho} & \text{if } r < R_{\bar{\nu}_e}^\epsilon \\ -\left[\frac{\partial L_{\nu_e}}{\partial r} + \frac{\partial L_{\bar{\nu}_e}}{\partial r}\right] \cdot \frac{1}{4\pi r^2 \rho} & \text{if } r > R_{\nu_e}^t \end{cases} \tag{59}$$

$$\dot{Y}_e = \begin{cases} \left[\frac{\partial L_{\bar{\nu}_e}^{N,\text{diff}}}{\partial r} - \frac{\partial L_{\nu_e}^{N,\text{diff}}}{\partial r}\right] \cdot \frac{m_b}{4\pi r^2 \rho} & \text{if } r < R_{\bar{\nu}_e}^\epsilon \\ \left[\frac{\partial L_{\bar{\nu}_e}^{N}}{\partial r} - \frac{\partial L_{\nu_e}^{N}}{\partial r}\right] \cdot \frac{m_b}{4\pi r^2 \rho} & \text{if } r > R_{\nu_e}^t \end{cases} \tag{60}$$

2.3.5 Spline Interpolation of Transition Region

In implementing the luminosity estimation schemes, there is a bit of inconsistency in when and where luminosity calculations may start, since the particular **choice** of neutrinosphere used in the integration ranges of r_o, r, and r' used in Equation 47 would all yield greatly disparate results. Case studies were performed which sought out the most physically representative scenario.

Given these imperfections in the luminosity estimation scheme, it made sense to isolate the radial grid where problems could occur where one species was accounted for and the other not, as number luminosity estimation calculations can only begin in front of radii where the Fermi-Dirac blackbody "light bulb" condition is set (and not within). I will be referring to the radial region as the **transition region**. Thus, of the four radii of interest ($R_{\nu_e}^\epsilon$, $R_{\bar{\nu}_e}^\epsilon$ $R_{\nu_e}^t$ $R_{\bar{\nu}_e}^t$), it was noted that their magnitude in time had a consistent hierarchy, constraining them into the following order throughout the simulation (corroborated by Figure 28):

$$\boxed{R_{\bar{\nu}_e}^\epsilon < R_{\bar{\nu}_e}^t < R_{\nu_e}^\epsilon < R_{\nu_e}^t} \tag{61}$$

- As $R_{\nu_e}^t$ was universally the outer most radius in the calculations, it became the point where both electron neutrinos and anti-neutrinos in the free-streaming limit were accounted for.
- As $R_{\bar{\nu}_e}^\epsilon$ was the innermost radius, it made sense to end the inner diffusive regime here for ν_e.

Although it could potentially continue for some grid points for $\bar{\nu}_e$, it would not have made physical sense to only account for one type of particle species and not the other. Thus, a cubic spline interpolation routine was written to essentially blend the two physical regimes. This is the motivation behind the radial range considered in Equations 59 and 60. The cubic spline interpolation scheme was inspired by examples shown in Pang [2006] and modified to accommodate the various inputs and variables of the NODALEP scheme.

3 Results and Analysis

3.1 Results of Neutrino Characterization via NODALEP

3.1.1 Neutrino Energetics

Output from Agile-IDSA in the form of luminosity and temperature allows us to post-process neutrino mean energy to quantify its magnitude. Figures 15 and 16 serve as an example to show $\langle\epsilon_1\rangle$, $\langle\epsilon_2\rangle$, and $\langle\epsilon_3\rangle$ (as derived in Section 2.2.1) at 120 ms post-bounce.

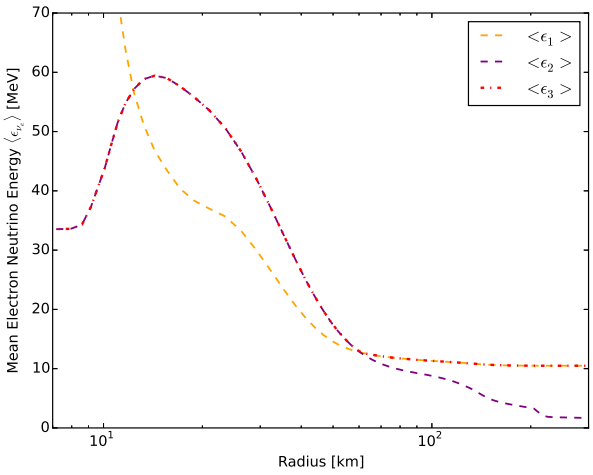

Figure 15: ν_e Mean Energy Profiles at 120 ms p.b.

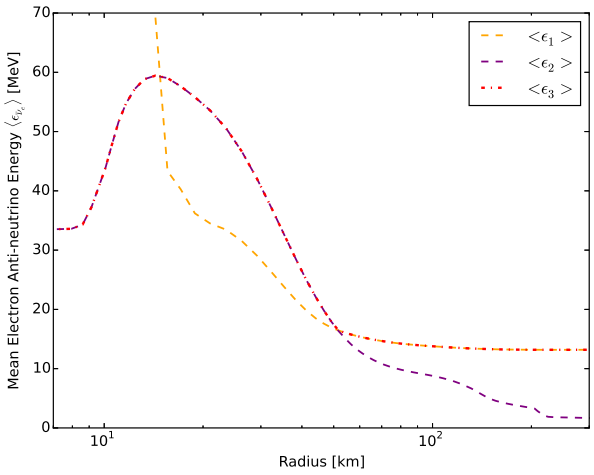

Figure 16: $\bar{\nu}_e$ Mean Energy Profiles at 120 ms p.b.

Calculation of $\langle\epsilon_2\rangle$ for both figures was performed using $\eta_\nu = 0$ and matter temperature T, as this is a good, first approximation for the transition point between neutrino thermal equilibrium and thermal decoupling. $\langle\epsilon_1\rangle$ was calculated using the neutrino number and energy luminosity outputted from IDSA. As described in Section 2.2.1, $\langle\epsilon_3\rangle$ is the "compromise" which uses both data sets to account for ϵ_ν at any radial point.

As stated previously, the assumption of $\eta_\nu = 0$ to represent accurate neutrino energies in the core of the PNS is false, as β equilibrium is quite accurate here. Large positive values for η_{ν_e} and large negative values for $\eta_{\bar{\nu}_e}$ tend to exaggerate the temperature profile inside of the PNS core ($r < 20$ km) and yield values for $\langle\epsilon_\nu\rangle$ on the order of 100-200 MeV. This inconsistency I am actually ignoring for the purposes of this section, as I wish to illuminate and concentrate on mean energies near to, and after, the energy neutrinosphere. Both cases of $\eta_\nu \neq 0$ and $\eta_\nu = 0$ will yield to a decrease and eventual failure of the Fermi-Dirac description after thermal decoupling and an eventual transition to a $\langle\epsilon_1\rangle$-dominated energy regime.

Additionally, by showing the radial dependence of both $L_\nu(r)$ and $L_\nu^N(r)$, it is worth illustrating to the reader the stabilization and consistency of the values for both in the free-streaming region. This implies that neutrinos which may be observed by a neutrino detector on Earth or in space (in the future) effectively tell the story of where (and potentially when) in the PNS environment they were emitted on account of their energy amplitude. Since energy-exchanging interactions at some point become more infrequent, due to decreasing medium density and thus neutrino opacities, additional changes in energy and number luminosity occur less frequently as neutrinos move to less opaque regions ($\tau_\nu \ll 1$). As L_ν has units of [MeV/s] and L_ν^N has units of [#/s], yielding the depicted units of mean energy for $\langle\epsilon_1\rangle$ in the figures. Simply by reading off Figures 15 and 16 again as a reference, we can note the actual points of thermal or energetic decoupling at $r \approx 60$ km for electron neutrinos $\boldsymbol{\nu_e}$ and $r \approx 50$ km for electron anti-neutrinos $\boldsymbol{\bar{\nu}_e}$, which reflects their behavior specifically at 120 ms post-bounce in the post-processing of this simulation.

3.1.2 Mean Free Path λ_ν, Optical Depth τ_ν, Neutrinosphere from τ_ν, Flux Factor

Mean Free Path Results

In seeking to better understand the output of Agile-IDSA's neutrino transport, we recall Equation 7 which shows how λ_ν is calculated in the IDSA. Looking deeper into IDSA's spectral treatment of neutrino energies, I find that twenty energy bins are used by default. As the range of energies are fixed (and separated logarithmically) at these twenty discrete values with values at each radial shell of the simulation (102 by default), this yields $102 \times 20 = \mathbf{2040}$ values for the

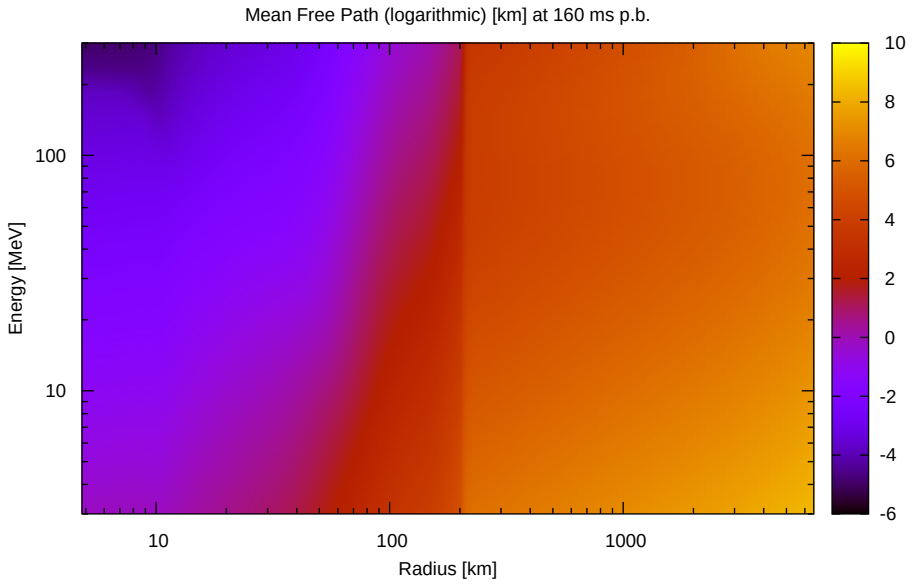

Figure 17: Electron Neutrino Mean Free Path $\lambda_{\nu_e}(\epsilon, r)$ at 160 ms p.b. in [km]

mean free path at any given time step. Figure 17 illustrates (using a color map) the multi-dimensional nature of λ_ν's dependence on both neutrino energy ϵ and the local position on the radial grid (i.e radius r):

This color map shows the logarithmic power value of the mean free path for electron neutrinos $\lambda_{\nu_e} = \lambda_{\nu_e}(\epsilon, r)$, illustrating the contribution of both the neutrino cross-section and the number density of baryonic targets from Equation 24.

The propagating shock wave has its maximum near 200 km in this figure and is depicted as a sharp gradient in λ_{ν_e}. Additionally, although not as sharp, one can note the skewed fuchsia diagonal line with positive slope starting at about 40 km and leading upwards to about 200 km, which is a visual representation of $R^t_{\nu_e} = R^t_{\nu_e}(\epsilon_\nu)$. This is where $\tau_{\nu_e}(R^t_{\nu_e}(\epsilon_\nu)) = 2/3$ for every energy bin and represents the soft, "fuzzy" transition between the optically thick ($\tau_{\nu_e} \gg 1$) and optically thin ($\tau_{\nu_e} \gg 1$) regions.

For the sake of numerical simplicity (i.e. avoiding working with 2040 values of λ_ν and instead opting for 102, or one per radial zone) and an added tangibility of the meaning of neutrino energy, we reintroduce the consideration of the mean energy. We know that $\langle \epsilon_\nu \rangle$ will probably not be exactly one of the twenty values of energy bins provided by the IDSA, but must be located somewhere in this range (3 MeV to 300 MeV as set by default in IDSA). The desired, representative mean free path $\lambda_\nu(\langle \epsilon \rangle)$ must then be interpolated to determine a mean free path which would correspond to that particular value of mean energy $\langle \epsilon_\nu \rangle$ (i.e.). Linear interpolation was used in this calculation, as the variation of λ_ν from point-to-point was fairly regular (in a log-log scaling), as shown in Figure 18.

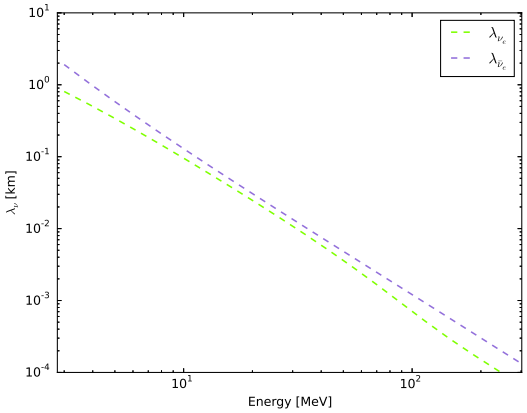

Figure 18: λ_ν for Arbitrary Fixed Shell Zone and Time Step

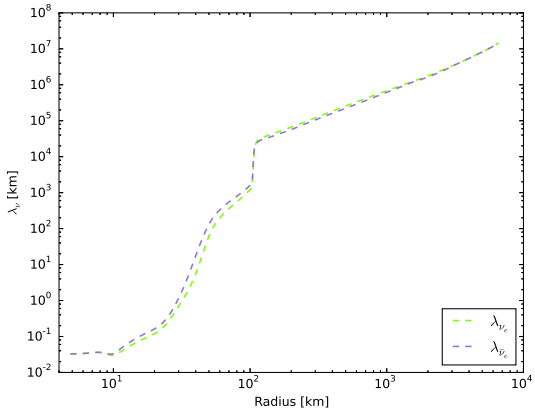

Figure 19: λ_ν for Arbitrary Fixed Energy Bin and Time Step

For a fixed radial shell zone and time step, Figure 18 (in a log-log scale) effectively highlights the consequences of $\lambda_\nu \propto 1/\epsilon_\nu^2$, which stems from the relation: $\sigma_\nu \propto \epsilon_\nu^2$. Indeed, it is known (see Bethe [1990], for example) that neutrinos of higher energy have a shorter mean free path. Figure 19 illustrates the mean free path of a neutrino assuming it is produced at a given radius. Figure 19 may give the false impression that λ_ν is dependent on radius in a strict one-to-one fashion. In actuality, λ_ν is dependent on the local properties of matter (as corroborated by Equation 24), so should be analyzed with this in mind. The jump after about 100 km corresponds to the shock wave location at this arbitrary time step.

Optical Depth Results

Using the discretized form of τ_ν (Equation 30), it is possible to determine the optical depths for both $\boldsymbol{\nu_e}$ and $\boldsymbol{\bar{\nu}_e}$. The dashed line in Figures 20 and 21 represents an optical depth of 2/3, which is useful in defining per convention (see Equation 6.12, Bethe [1990]) the neutrinosphere of the PNS environment. This particular neutrinosphere is the *transport* sphere R_ν^t due to IDSA's output of the usage of this quantity by default. In NODALEP, both transport and effective neutrinospheres are considered for each species, yielding four unique quantities which can be attributed to optical depth τ_ν.

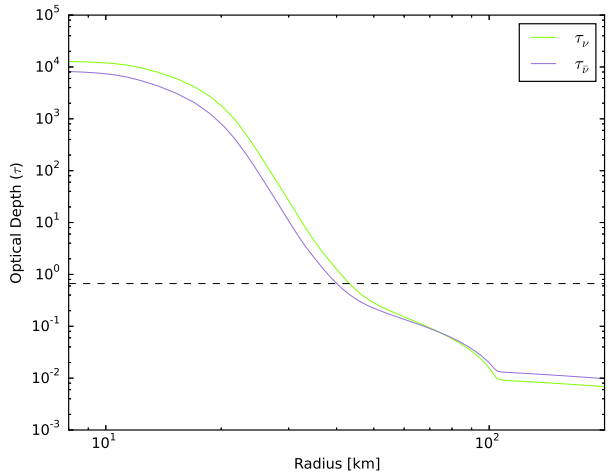

Figure 20: τ_{ν_e} and $\tau_{\bar{\nu}_e}$ for 450 ms p.b.

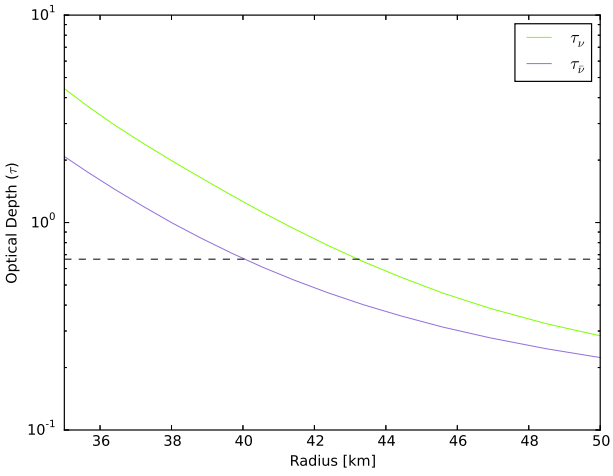

Figure 21: τ_{ν_e} and $\tau_{\bar{\nu}_e}$ for 450 ms p.b. (magnified)

From the magnified plot in Figure 21, the transport neutrinospheres can be read off as $R_{\nu_e}^t \approx 43$ km and $R_{\bar{\nu}_e}^t \approx 40$ km, which are different[8] values from that of the energetic decoupling points in Section 2.2.1 $\left(R_\nu^t \neq R_\nu^\epsilon\right)$. We see that the transport neutrinosphere R_ν^t for electron neutrinos is larger than that of electron anti-neutrinos, as was similarly noted for the energy neutrinosphere R_ν^ϵ in Section 2.2.1. When considering the reciprocal $1/\lambda_\nu \propto E_\nu^2$ term in the optical depth integration juxtaposed with Figure 21 at a fixed arbitrary radius, we see that $\tau_{\nu_e} > \tau_{\bar{\nu}_e}$. This is explained by the fact that **electron anti-neutrinos decouple from baryonic matter sooner from their transit from the core to the outside than electron neutrinos**. This is also why their spectra have higher energy [Janka, 1995]. As $\boldsymbol{\bar{\nu}_e}$ depend on protons for absorption, it is clear that $\boldsymbol{\nu_e}$ interact more copiously as their absorption probability depends solely on neutrons, contributing to opacity more readily.

Flux Factor Results

The method for obtaining flux factors was described in the context of the luminosity estimation scheme (NODALEP) shown previously, where the term $\langle\mu_\nu\rangle$ (not to be confused with chemical potential), addresses the geometric anisotropy of neutrino propagation. After applying the described fit from Liebendörfer et al. [2009], we were able to obtain values for $\langle\mu_\nu\rangle$ which agree extremely well with those seen in Janka [1991] (see Figure 2 in this reference).

In Figures 22 and 23, we show the profiles of the flux factor used in our code, which is based on the fitting formula in Liebendörfer et al. [2009], which is also used by IDSA. To conform to the requirements of the fit, $\langle\mu_\nu\rangle$ is equal to $^1/_4$ at the transport neutrino sphere R_ν^t (and within as well) yet must approach unity as $r \to \infty$. Figures 22 and 23 show these factors at two separate times, for both electron neutrino species, with transport neutrinospheres shown as well.

[8] A gross simplification made by some studies of supernova simulations equates these two separate neutrinospheres. No such assumption is made in this work and is indeed a motivation for this investigation.

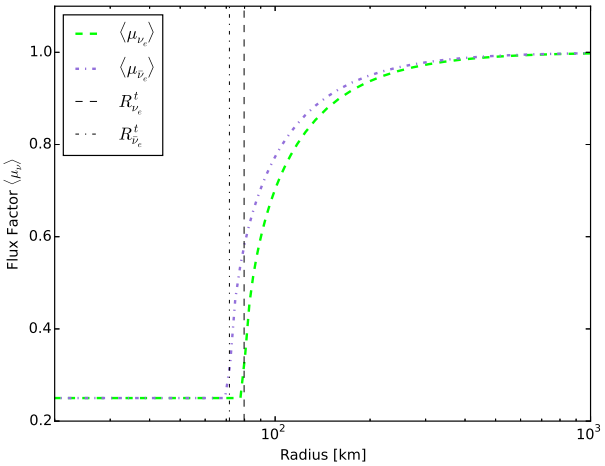

Figure 22: Flux Factor vs. Radius (20 ms p.b.)

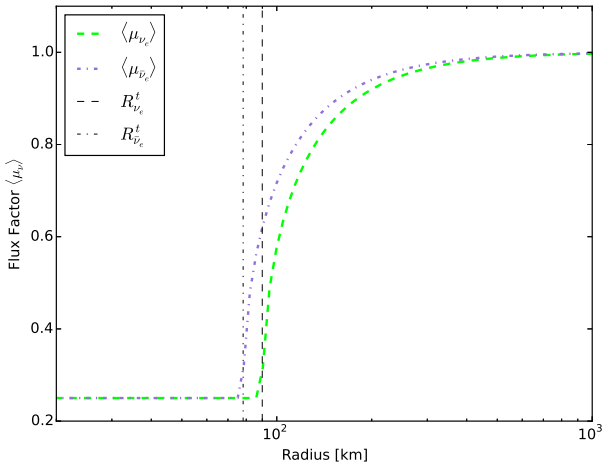

Figure 23: Flux Factor vs. Radius (70 ms p.b.)

3.1.3 Heating & Cooling, Blackbody Luminosity, Neutrino Degeneracy & Gain Region

Heating & Cooling

Figures 24a − 24d depict the profiles for heating and cooling contributions from both electron neutrinos and anti-neutrinos together, in terms of the specific energy rate $q^{\pm}_{\nu}$ (recall that $q^{\pm}_{\nu} = Q^{\pm}_{\nu}/\rho$). Similar to the presented Agile-IDSA result, this model does not take heating and cooling due to heavy neutrinos $\boldsymbol{\nu_x}$ into account. The figures show the competitive development of heating and cooling at two sample time steps and use the species total ($Q^{\pm}_{\nu} = Q^{\pm}_{\nu_e} + Q^{\pm}_{\bar{\nu}_e}$) of the models introduced in Section 2.2.3.

In addition to the exact-form models already seen, Janka [2001] also shows approximate forms for both Q^{+}_{ν} and Q^{-}_{ν}, which make broad assumptions to recover simpler, more compact forms of Equations 33 - 36 which depend on fewer simulation inputs:

$$Q^{+}_{\nu} \approx 160 \cdot \frac{\rho}{m_u} \cdot \frac{L_{\nu_e,52}}{r_7^2 \cdot \langle\mu_\nu\rangle} \cdot \left(\frac{k_B T_{\nu_e}}{4\ \text{MeV}}\right)^2 \qquad Q^{-}_{\nu} \approx 145 \cdot \frac{\rho}{m_u} \cdot \left(\frac{k_B T}{2\ \text{MeV}}\right)^6$$

where r_7 is the radius in units of 10^7 cm and $L_{\nu_e,52}$ is the neutrino luminosity normalized to 10^{52} erg/s. The most notable differences between q^{-}_{exact} : Janka (2001) and q^{-}_{approx} : Janka (2001) at 100 ms p.b. are in the gain region $R_g < r < R_s$. Although both total cooling quantities predict similar gain radii when intersected with q^{+}_{exact} : Janka (2001), it is q^{-}_{approx} : Janka (2001) which may make it artificially seem as though heating is higher in this regime, by assuming $F_5(0)$ too early. Janka refers to this as a good assumption in the gain region, but only at later times, as in Figure 24d. Figures 24e and 24f show how the values of η_{e^-} and η_{e^+} change throughout the PNS radial profile at different times. The reader should keep in mind that the 5th order Fermi-Dirac integral function seen in the exact forms for Janka's cooling (Equations 35 & 36), can create meaningful, large differences (even in a log-log scale) between a null and non-zero argument, and thus affect the amplitude of the cooling term (e.g. at 20ms p.b η_{e^-} spikes to 5, which comparatively yields $F_5(5)/F_5(0) \sim 100$, or two whole orders of magnitude greater!). Usage of the approximate form in the first 100-200 ms post-bounce is therefore not recommended.

To essentially verify and compare the strength of the Janka-based neutrino cooling Q^{-}_{ν} term, we used the nprates subroutine in Agile-IDSA to post-process and determine neutrino emissivity $j_{\text{IDSA}}(\epsilon)$ due to neutrino emission from interaction with free nucleons at a given input of ρ, T, Y_p, Y_n, μ_e, and $\hat{\mu}$ (to account for nucleon degeneracy corrections at high densities). Using the neutrino emissivity, it is then possible to construct a cooling rate from nprates (which also accounts for Pauli blocking), discretely summed up over *ne* energy bins with:

$$Q^{-}_{\text{IDSA}} = \frac{4\pi}{(hc)^3} \cdot c \cdot \int_0^{+\infty} d\epsilon \cdot \epsilon^3 \cdot j_{\text{IDSA}}(\epsilon) \approx \frac{4\pi}{(hc)^3} \cdot c \cdot \sum_{i=1}^{ne} d\epsilon_i \cdot \epsilon_i^3 \cdot j_{\text{IDSA}}(\epsilon_i) \tag{62}$$

provided $j_{\text{IDSA}}(\epsilon)$ is in units of cm^{-1}, Q^{-}_{IDSA} gets converted from [$\text{MeV} \cdot \text{s}^{-1} \cdot \text{cm}^{-3}$] to [$\text{erg} \cdot \text{s}^{-1} \cdot \text{cm}^{-3}$] (as the Janka expression is in the latter units), and finally is expressed as $q^{-}_{\text{IDSA}} = Q^{-}_{\text{IDSA}}/\rho$ for direct comparison with the Janka

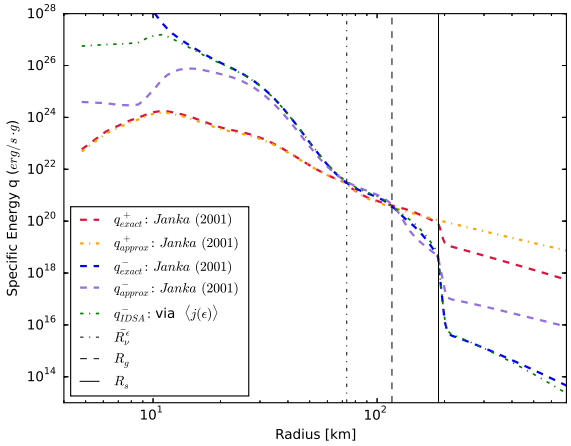

(a) $\nu_e/\bar{\nu}_e$ Heating and Cooling (100 ms p.b.)

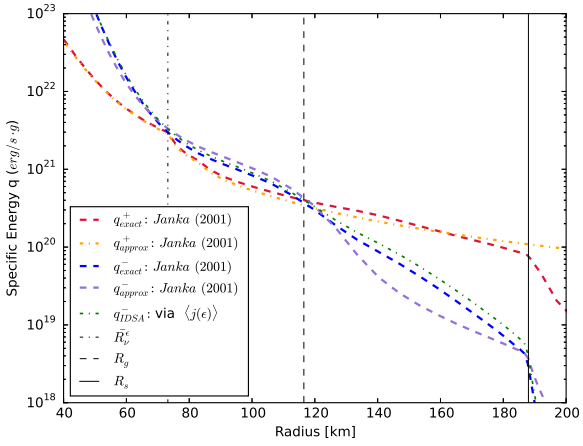

(b) Magnified (100 ms p.b.)

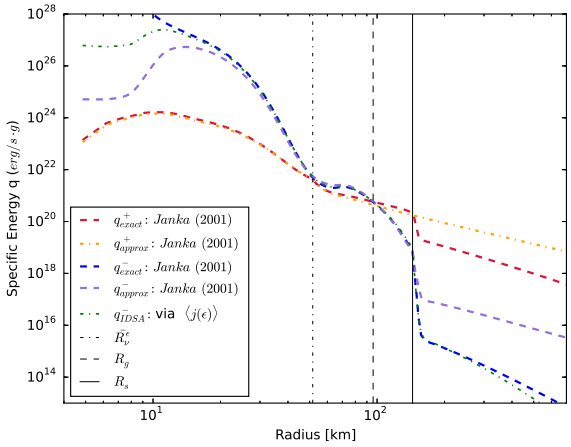

(c) $\nu_e/\bar{\nu}_e$ Heating and Cooling (300 ms p.b.)

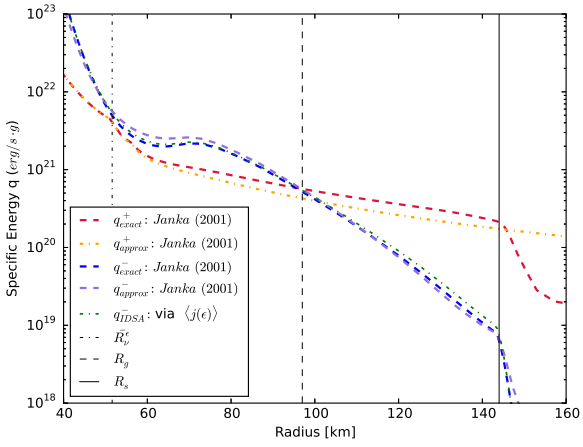

(d) Magnified (300 ms p.b.)

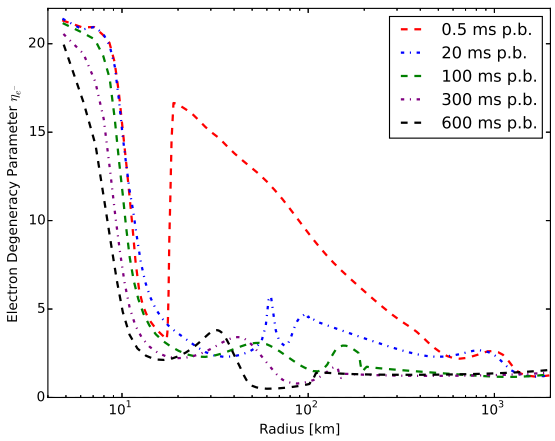

(e) Electron Degeneracy Parameter

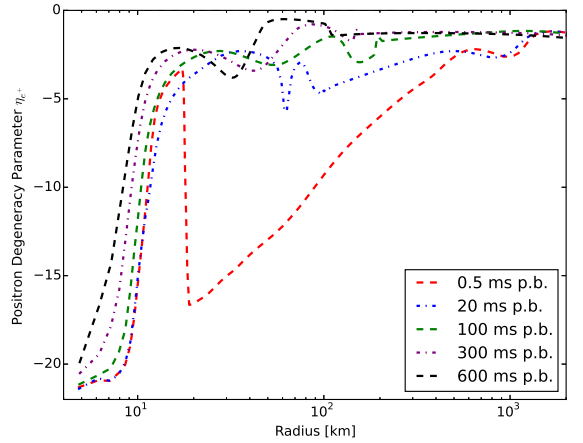

(f) Positron Degeneracy Parameter

Figure 24: Heating and Cooling Profiles

formulas. Any differences seen in Figure 24 are insignificant until outside the shock radius R_s or deep within the proto-neutron star. For our purposes in the gain region ($R_\nu < r < R_s$), these minor differences can be neglected.

Black-Body Light Bulb

As we made an estimation on the point at which neutrino and matter energies decoupled in the aforementioned simulation of a 15 $M_\odot$ star, we may then use Equation 46 to set a boundary condition for the radial luminosity profile of the system. Based on theory, this value should approximate the Fermi-Dirac black-body luminosity L_ν^{FD} of the proto-neutron star at or very near R_ν^ϵ. What happens after? To assess this behavior, it is necessary to see what role neutrinos play in the heating and cooling of the proto-neutron star environment.

As depicted in Figure 25 and corroborated by Equation 46, the values of $L_\nu^{N,FD}$ and L_ν^{FD} are *highly* dependent on η_ν, T and r. The curve in red assumes that the neutrino degeneracy parameter η_ν for electron neutrinos is zero (and consequently also for anti-neutrinos, as $\eta_{\nu_e} \approx \eta_{\bar{\nu}_e}$ as $\eta_{\nu_e} \to 0$. The curves in green and purple assume η_ν is in β equilibrium, which yields one value for η_{ν_e} and another for $\eta_{\bar{\nu}_e}$. Beta equilibrium is explained in more detail in the following section.

Near the neutrinosphere, Figure 26 illustrates how well Agile-IDSA's output of neutrino luminosity compares to the Fermi-Dirac light bulb which has been calculated in post-processing given these three inputs alone. With no more than 5 - 10 B/s deviation in the vicinity of the transport neutrinosphere, the luminosity is therefore well approximated. Thus, it is important that the calculations in NODALEP which consider Fermi function values in their calculations actually use a realistic approximation.

$$L_\nu^{N,FD}(r) = \frac{4\pi^2}{c^2 h^3} \cdot r^2 \cdot T^3(r) \cdot \mathcal{F}_2(\eta_\nu)$$
$$L_\nu^{FD}(r) = \frac{4\pi^2}{c^2 h^3} \cdot r^2 \cdot T^4(r) \cdot \mathcal{F}_3(\eta_\nu) \tag{63}$$

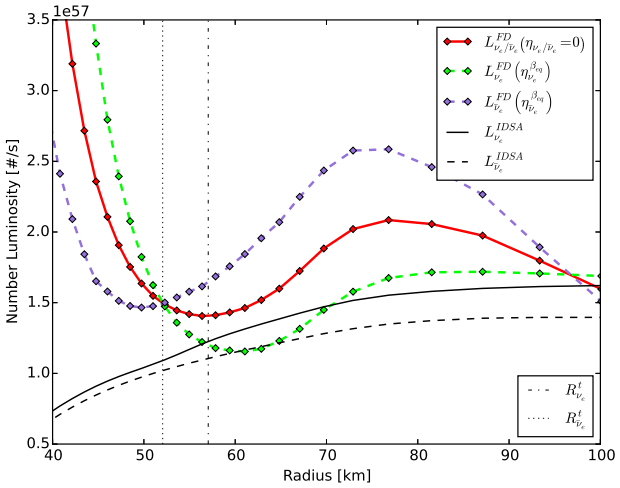

Figure 25: Number Light Bulb Candidates at 300 ms p.b.

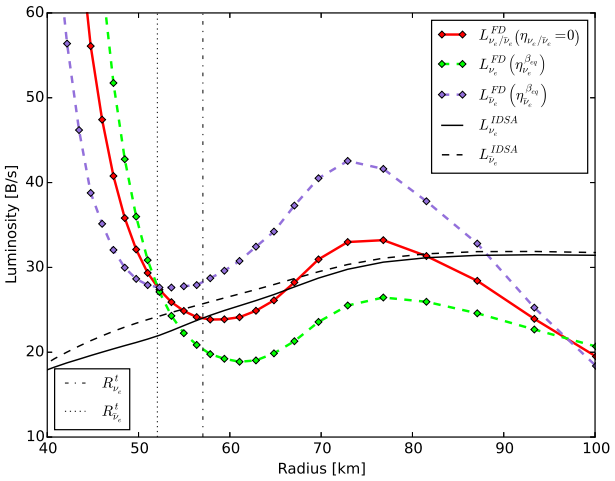

Figure 26: Energy Light Bulb Candidates at 300 ms p.b.

As we can see from the figures, although β equilibrium is accurate at high temperatures and high density, the assumption of zero degeneracy for neutrinos is actually good, and indeed better, than the rigorous assumption of constructing the neutrino degeneracy parameter for the determination of the Fermi-Dirac black-body light bulb. Beta equilibrium is, on the other hand, very accurate in the aforementioned regimes and is thus worthwhile to consider for other applications.

Neutrino Degeneracy Parameter

In many of the calculations, we use formulations which depend on the value of the neutrino degeneracy parameter η_ν. This is a direct result of assuming a Fermi-Dirac distribution. Often times, this is taken to be zero, as this is a good approximation in some regions of the PNS (see Figures 27a - 27d). How good of an assumption is this?

Aside from the fact that η_ν happens to be close to zero under certain conditions and is easier to calculate, the primary motivation for assuming $\eta_\nu = 0$ is that it saves us from making assumptions. One assumption that we can make with confidence is that of **β equilibrium**. In β equilibrium, beta decay is in perfect equilibrium with their exchange hadrons through charged-current interactions. Assuming the chemical potentials are equilibriated:

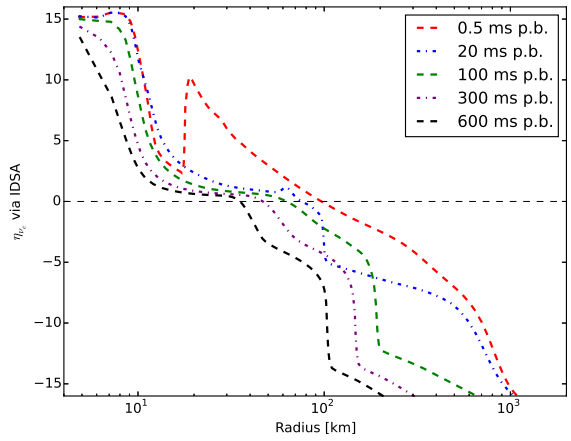

(a) Neutrino $\eta_{\nu_e}^{\mathrm{IDSA}}$ vs. Radius

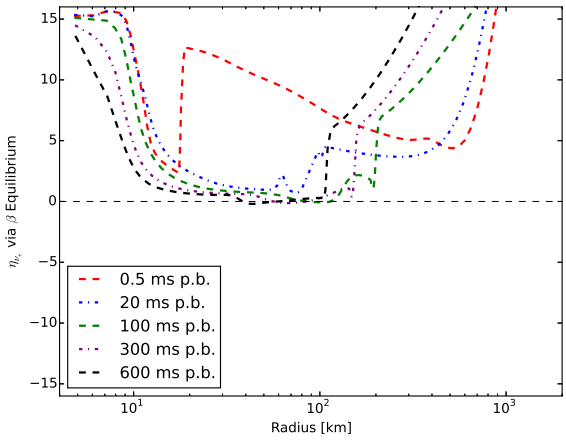

(b) Neutrino $\eta_{\nu_e}^{\beta_{\mathrm{eq}}}$ vs. Radius

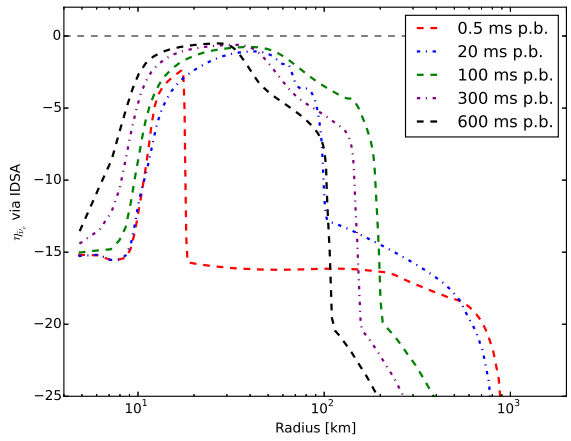

(c) Anti-Neutrino $\eta_{\bar{\nu}_e}^{\mathrm{IDSA}}$ vs. Radius

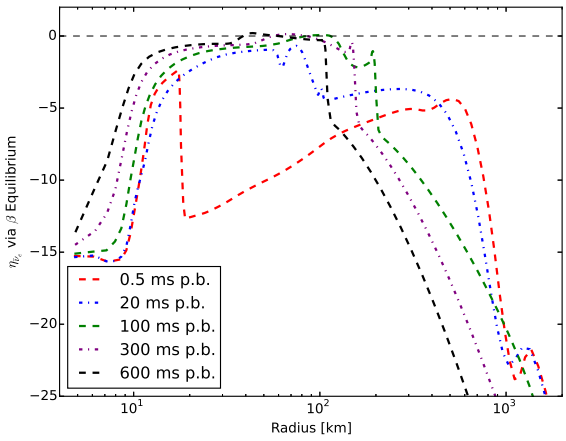

(d) Anti-Neutrino $\eta_{\bar{\nu}_e}^{\beta_{\mathrm{eq}}}$ vs. Radius

Figure 27: Evolution of Neutrino Degeneracy over Time: IDSA vs. β Equilibrium

$$e^- + p \longrightarrow \nu_e + n \quad \Longrightarrow \quad \mu_{e^-} + \mu_p = \mu_{\nu_e} + \mu_n \quad \Longrightarrow \quad \mu_{\nu_e} = \mu_e - \hat{\mu} - \Delta_{np} \quad \Longrightarrow \quad \eta_{\nu_e} = \frac{\mu_{\nu_e}}{T}$$

$$e^+ + n \longrightarrow \bar{\nu}_e + p \quad \Longrightarrow \quad \mu_{e^+} + \mu_n = \mu_{\bar{\nu}_e} + \mu_p \quad \Longrightarrow \quad \mu_{\bar{\nu}_e} = -\mu_e + \hat{\mu} + \Delta_{np} \quad \Longrightarrow \quad \eta_{\bar{\nu}_e} = \frac{\mu_{\bar{\nu}_e}}{T}$$

where $\hat{\mu} = \mu_n - \mu_p$ as in Bethe [1990], $\Delta_{np} = 1.29$ MeV is the correction for the rest mass-energy difference between a neutron and a proton, and for electron anti-neutrinos, $\eta_{\bar{\nu}_e} = -\eta_{\nu_e}$. The usage of $\hat{\mu}$ is made possible by a call to the EOS, and makes the quantities at non-zero η_ν plausible to calculate with the assumption of β equilibrium. Figures 27a - 27d show the differences between the η_{ν_e} and $\eta_{\bar{\nu}_e}$ obtained directly from the post-processed value of η_ν from IDSA vs. the η_ν which can be constructed by using μ_e and $\hat{\mu}$ called from the EOS, by assuming β equilibrium, and utilizing the matter temperature T: for electron neutrinos $\eta_{\nu_e} = \left(\mu_e - \hat{\mu} - \Delta_{np}\right)/T$ and electron anti-neutrinos $\eta_{\bar{\nu}_e} = \left(-\mu_e + \hat{\mu} + \Delta_{np}\right)/T$. For the range where ν_e and $\bar{\nu}_e$ are trapped and in thermal equilibrium with matter, β equilibrium agrees quite well with the IDSA result at many time steps.

The differences shown in the corresponding figures start to deviate rather strongly after the shock radius R_s and can no longer accurately represent proper neutrino characteristics. Fortunately, all calculations requiring a solution of $\mathcal{F}_n(k)$ are within $0 < r < R_s$ and can be decomposed into two hierarchies: $i.)$ those which take $\eta_\nu = 0$ or $ii.)$ those which take $\eta_\nu = \eta_\nu^{\beta_{eq}}$ at beta equilibrium. The gradient between these two regions should also be interpolated, to retain a smooth transition. This kind of "compromise" was also suggested in Ruffert et al. [1996] and should be used by any future neutrino transport scheme for calculations which require a neutrino degeneracy parameter!

3.2 Advanced Results of NODALEP

3.2.1 Evolution of Neutrinospheres

The evolution of the neutrino spheres is a critical validation of any neutrino transport. Through the emission of neutrinos and anti-neutrinos, a proto-neutron star loses energy. Indeed, over 99% of the gravitational binding energy gained as potential energy due to core-collapse is re-emitted by neutrinos (see Woosley et al. [2002]). The successive cooling of the proto-neutron star eventually leads to final state neutron stars which can have a maximum mass in the range of $M_{NS,\max} \sim 2.0\ \mathrm{M}_\odot$. Lattimer and Prakash [2001] show that a strong correlation between neutron star mass and radius exists, and extrapolation of calculated neutrinospheres, for example, can give clues as to what the proto-neutron surface radius will look like in the seconds and minutes after core-collapse. Post-processing of neutrino-wind simulation data by Yasin [2013] shows the neutrinospheres already on the same order of magnitude as the expected final-state neutron star radius (10 km - 15 km) in the first several seconds of PNS cooling. The rate of neutrino cooling depending on the equation of state, total mass of the proto-remnant, heavy neutrino physics (annihilation & pair production), and other secondary variables. This suggests neutrino cooling plays quite a hearty role in the evolution of a neutron star in the seconds following collapse, bounce and shock propagation.

To assess the overall neutrino cooling in our simulation, neutrinospheres at each time step were collected in post-processing and written to a file. Figure 28 suggests a maximum in the neutrinospheres at about 70 - 75 ms post-bounce due to a rush of increased opacity from free nucleons being accreted from the shock to the neutrinosphere "surface" at $\tau_\nu = 2/3$, which grows temporarily at this stage of evolution.

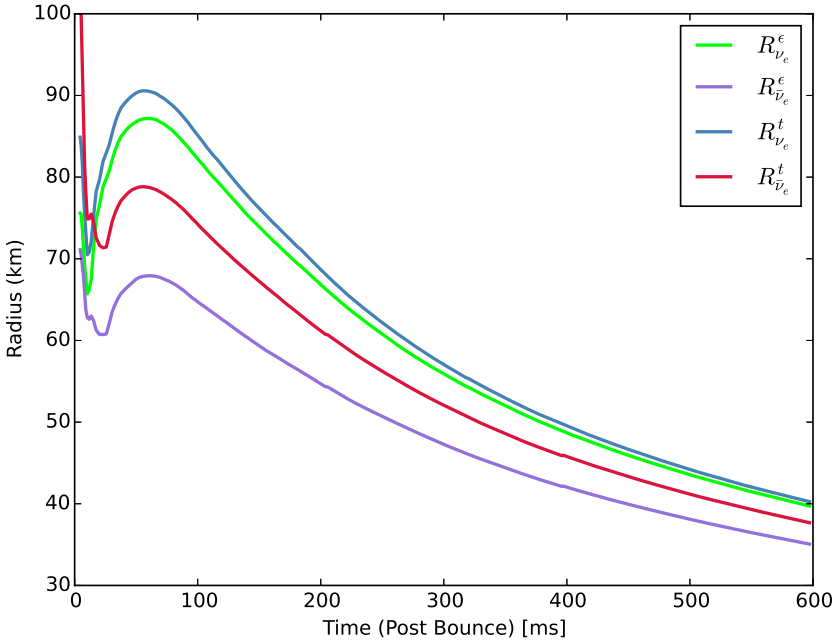

Figure 28: Neutrinosphere Evolution in Time from NODALEP

3.2.2 Luminosities from NODALEP

The neutrino number and energy luminosities stand to be one of the most trying quantities to capture for any neutrino transport, grey and spectral alike. Calculating this quantity using a grey transport scheme and expecting the comparison to agree well with IDSA's spectral approach is unrealistic. Despite initial reservations, it was already apparent from Liebendörfer et al. [2005] that there would be some differences between a spectral Boltzmann equation solution and a spectral diffusive source approximation in IDSA, not to mention a spectral and grey approximation.

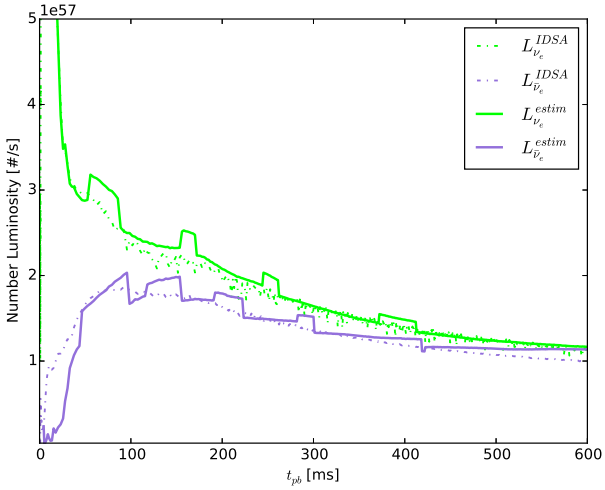

Figure 29: Number Luminosity Estimates: IDSA vs. NODALEP

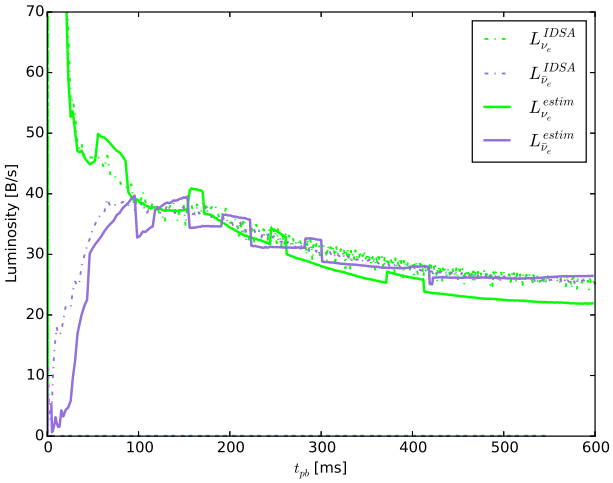

Figure 30: Energy Luminosity Estimates: IDSA vs. NODALEP

Figures 29 and 30 represent the effective luminosity (number or energy) which can be seen at $r \to \infty$, or in other words, what comes out of the proto-neutron star's atmosphere. This is then the aggregate value of all the absorption and re-absorption which has taken place in all previously traversed radial zones (compare to Figure 12). The estimation of this luminosity is also a litmus test to see if a neutrino transport scheme is reproducing the expected qualitative behavior. We attribute the good agreement in the number luminosity to properly selecting a Fermi-Dirac blackbody light bulb,

expressing dampening and re-absorption using accurate neutrino opacities for κ_{abs} and a good value for the flux factor μ_ν.

An additional note is the jagged behavior of Figures 29 and 30, which could be an artifact created by the mapping of the interpolated neutrinosphere onto a definite grid index. It's clear that the fluctuation due to this artifact is not something that grows in time.

3.2.3 Results of Specific Energy Rate $\dot{e}$ Analysis and Change of Electron Abundance $\dot{Y}_{\text{e}}$ Results

Despite being a grey transport scheme, NODALEP actually does reproduce key features and properties of both $\dot{e}$ and $\dot{Y}_e$ profiles. The specific energy rate $\dot{e}$ was computed for the entire radial range as described in Sections 2.3.3, 2.3.4, and 2.3.5. Figures 31a, 31c, 31e, 31g show how this evolves in time. The cooling region from $\dot{e}_{NODALEP}$ is well approximated, but $\dot{e}$ in the heating region is consistently lower than in the estimation scheme. This could be due to either too low neutrino luminosity from the cooling region, a mischaracterization of the neutrino square mean energy, or could be due to the non-spectral nature of NODALEP itself. Additionally, compared to IDSA, NODALEP's gain radius R_g (where $\dot{e} = 0$) is consistently further out, which confirms an overall lack of neutrino heating from the estimation scheme.

The comparison of $\dot{Y}_{\text{e}}$ also yields a generally reproduced behavior between the two curves, but with disagreements in particular at the boundary between the diffusive and spline interpolation regimes. The estimate in the free-streaming regime for $\dot{Y}_{\text{e}}$ is actually in good agreement with IDSA.

These calculations were also a good validation of the spline interpolation algorithm used to "connect" the $\dot{e}$ and $\dot{Y}_{\text{e}}$ points from the diffusive regime and the free-streaming regime. Depending on the time step, there were on average only 8-12 points (compared to a total of 102 points on the adaptive mesh grid) which fell into the jurisdiction of the spline interpolation region. Tests done with NODALEP showed that the routine indeed smoothened out and polynomially interpolated data of interest between the two radii of interest ($R^{\epsilon}_{\bar{\nu}_e}$ and $R^{t}_{\nu_e}$, the electron anti-neutrino energy sphere and the electron neutrino transport sphere respectively). This generalized spline interpolation was then used between these two radii using data from before $R^{\epsilon}_{\bar{\nu}_e}$ (representing the diffusion regime) and after $R^{t}_{\nu_e}$, where free-streaming was an appropriate definition *for both* $\boldsymbol{\nu_e}$ and $\boldsymbol{\bar{\nu}_e}$.

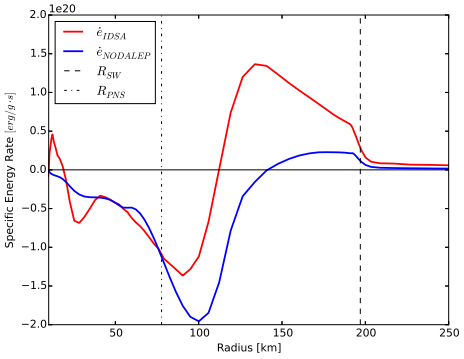

(a) $\dot{e}$ at 100 ms p.b.

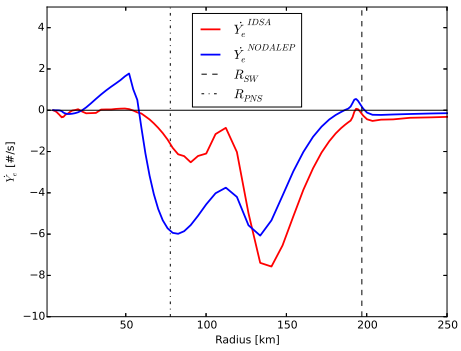

(b) $\dot{Y}_e$ at 100 ms p.b.

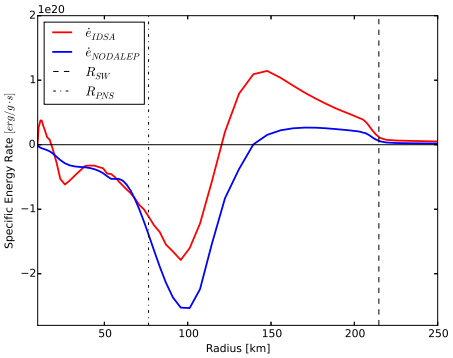

(c) $\dot{e}$ at 120 ms p.b.

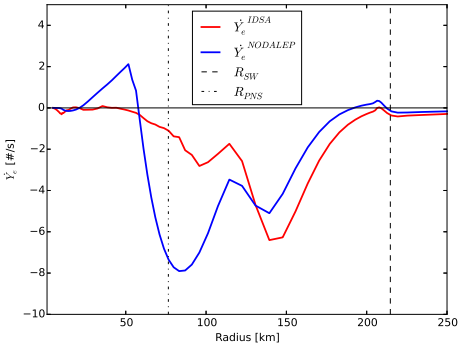

(d) $\dot{Y}_e$ at 120 ms p.b.

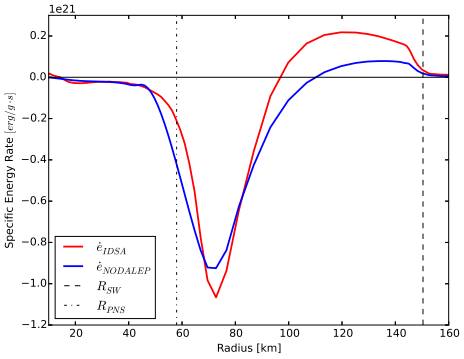

(e) $\dot{e}$ at 300 ms p.b.

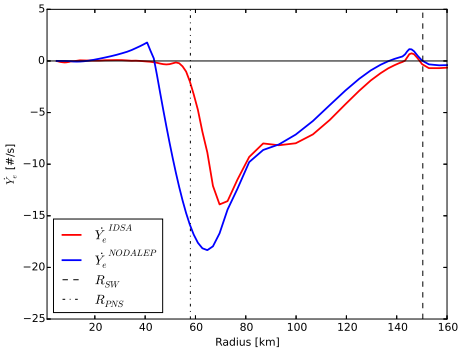

(f) $\dot{Y}_e$ at 300 ms p.b.

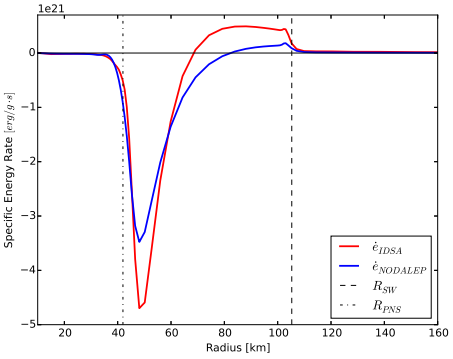

(g) $\dot{e}$ at 600 ms p.b.

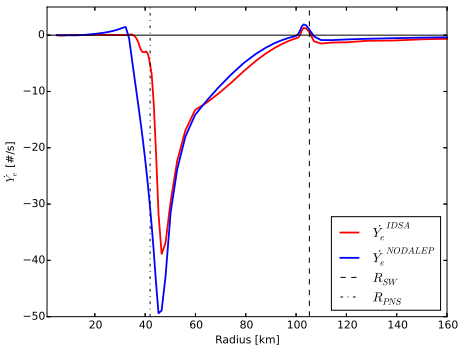

(h) $\dot{Y}_e$ at 600 ms p.b.

Figure 31: Comparison of $\dot{e}$ and $\dot{Y}_e$ from IDSA and NODALEP

4 Summary and Conclusions

Neutrinos (of all flavors) play a decisive role in the modeling of core collapse supernovae, as they carry away most of the energy released in the gravitational collapse of the iron core of a massive star (yielding a neutron star), within the first $\sim$ 10s after the collapse. In particular, neutrino absorption and emission above the surface of the accreting proto-neutron star is able to influence the explosion mechanism of a core-collapse supernova. While the prompt shock is always prone to fail due to energy loss in matter dissociation and neutrino emission, the re-absorption of a fraction ($\sim$ 10%) of the emitted neutrinos under the stationary accreting shock front can potentially revive the shock (neutrino-driven explosion mechanism). Moreover, neutrino interactions with matter determine the lepton and the electron fraction inside the proto-neutron star, as well as in the expanding layers. These quantities influence the subsequent matter evolution, especially the nucleosynthesis in the supernova ejecta.

The variety of thermodynamical conditions encountered in the core collapse scenario makes the modeling of neutrino transport extremely challenging, especially in multi-dimensional numerical simulations. This motivated the development of a large number of approximated transport schemes. For those simulations where general neutrino characterization is a secondary goal, it is rather sufficient to express neutrino quantities as energy averaged (using in other words, a grey scheme, as opposed to a spectral scheme). Indeed, referring to a mean energy is often more tangible and representative of the local behavior of neutrinos. Although not very accurate, the usage of such schemes allows one to more efficiently explore the effects of neutrinos and their mean energies on the explosion and on the subsequent nucleosynthesis, and enables the evolution of a CCSN simulation over longer timescales (i.e. more than a few seconds).

The aim of this thesis was to develop a new and efficient treatment for electron neutrinos and anti-neutrinos in the post-bounce phases of a core-collapse supernova. We called it NODALEP which stands for `Neutrino Optical Depth And Luminosity Estimation Program`. To this end, we used the open source Agile-IDSA code to explore the major features of a spherically symmetric core-collapse model, and to benchmark the estimates of our own model in a post-processing way. In particular, we considered the radial profiles (expressed in terms of matter density, temeprature and electron fraction) obtained by an Agile-IDSA simulation of a 15 solar mass progenitor, evolved up to $\sim$ 0.5s after core bounce. After having computed the neutrino mean free paths and optical depths, we determined the location of the neutrinospheres and we assumed black-body neutrino emission from them. Above those spheres, we evolved consistently the neutrino luminosities in the free-streaming regime, taking into account both emission and absorption processes. From the local variations of the number and energy neutrino luminosities, we computed the electron fraction and the internal energy variations, respectively. Inside the neutrino sphere, a simple diffusion prescription is assumed.

Although not a rigorous neutrino transport scheme, NODALEP reproduces major features visible in IDSA, especially in terms of the local variations of internal energy and electron fraction, and more globally, in terms of the number and energy luminosities. On the other hand, the results of this work seem to indicate that the subtle mechanism that can potentially lead to shock revival requires a more accurate spectral transport scheme. A future step will be to combine our approximation with an existing hydrodynamics code (such as Agile, GR1D, or FLASH), to provide radiation source terms. This will allow us to run long-time simulations to study neutrino heating in the mass accretion phase and the neutron star cooling at later times.

Bibliography

[1] H. A. Bethe. Supernova mechanisms. *Reviews of Modern Physics*, 62:801–866, 1990.

[2] H. A. Bethe and J. R. Wilson. Revival of a stalled supernova shock by neutrino heating. *The Astrophysical Journal*, 295:14–23, Aug. 1985. doi: 10.1086/163343.

[3] H. A. Bethe, G. E. Brown, and J. Cooperstein. Convection in supernova theory. *The Astrophysical Journal*, 322: 201–205, Nov. 1987. doi: 10.1086/165715.

[4] J. M. Blondin, A. Mezzacappa, and C. DeMarino. Stability of Standing Accretion Shocks, with an Eye toward Core-Collapse Supernovae. *The Astrophysical Journal*, 584:971–980, 2003.

[5] S. W. Bruenn. Stellar core collapse - Numerical model and infall epoch. *The Astrophysical Journal Supplement Series*, 58:771–841, Aug. 1985. doi: 10.1086/191056.

[6] A. Burrows. Colloquium: Perspectives on core-collapse supernova theory. *Reviews of Modern Physics*, 85:245–261, 2013.

[7] A. Burrows, S. Reddy, and T. A. Thompson. Neutrino opacities in nuclear matter. *Nuclear Physics A*, 777(0):356 – 394, 2006.

[8] S. M. Couch and C. D. Ott. Revival of The Stalled Core-Collapse Supernova Shock Triggered by Precollapse Asphericity in the Progenitor Star. *ArXiv e-prints*, Sept. 2013.

[9] C. Giunti and C. W. Kim. *Fundamentals of neutrino physics and astrophysics*. Oxford University Press, Oxford ;New York, 2007.

[10] H.-T. Janka. Implications of detailed neutrino transport for the heating by neutrino-antineutrino annihilation in supernova explosions. *Astromony & Astrophysics*, 244:378–382, Apr. 1991.

[11] H.-T. Janka. When do supernova neutrinos of different flavors have similar luminosities but different spectra? *Astroparticle Physics*, 3(4):377 – 383, 1995.

[12] H.-T. Janka. Conditions for shock revival by neutrino heating in core-collapse supernovae. *Astronomy & Astrophysics*, 368:527–560, 2001.

[13] H.-T. Janka. Explosion Mechanisms of Core-Collapse Supernovae. *Annual Review of Nuclear and Particle Science*, 62:407–451, 2012.

[14] H.-T. Janka and W. Hillebrandt. Monte Carlo simulations of neutrino transport in type II supernovae. *Astromony & Astrophysics Supplemental Series*, 78:375–397, June 1989.

[15] H.-T. Janka and W. Hillebrandt. Neutrino emission from type II supernovae - an analysis of the spectra. *Astromony & Astrophysics*, 224:49–56, Oct. 1989.

[16] H.-T. Janka and E. Mueller. Neutrino heating, convection, and the mechanism of Type-II supernova explosions. *Astromony & Astrophysics*, 306:167, Feb. 1996.

[17] W. Keil and H.-T. Janka. Hadronic phase transition at supranuclear densities and the delayed collapse of newly formed neutron stars. *Astronomy & Astrophysics*, (296):145–163, 1995.

[18] R. Kippenhahn and A. Weigert. *Stellar Structure and Evolution*. Springer Verlag, 1990.

[19] J. M. Lattimer and F. Douglas Swesty. A generalized equation of state for hot, dense matter. *Nuclear Physics A*, 535: 331–376, Dec. 1991. doi: 10.1016/0375-9474(91)90452-C.

[20] J. M. Lattimer and M. Prakash. Neutron Star Structure and the Equation of State. *The Astrophysical Journal*, 550: 426–442, Mar. 2001. doi: 10.1086/319702.

[21] R. J. LeVeque, D. Mihalas, E. A. Dorfi, and E. Müller. *Computational Methods for Astrophysical Fluid Flow*. Saas-Fee Advanced Course 27, Lecture Notes 1997. Springer Verlag, 1997. doi: 10.1007/3-540-31632-9.

[22] M. Liebendörfer. A Simple Parameterization of the Consequences of Deleptonization for Simulations of Stellar Core Collapse. *The Astrophysical Journal*, 633:1042–1051, 2005.

[23] M. Liebendörfer, S. Rosswog, and F.-K. Thielemann. An Adaptive Grid, Implicit Code for Spherically Symmetric, General Relativistic Hydrodynamics in Comoving Coordinates. *The Astrophysical Journal Supplement Series*, 141: 229–246, 2002.

[24] M. Liebendörfer, O. E. B. Messer, A. Mezzacappa, S. W. Bruenn, C. Y. Cardall, and F.-K. Thielemann. A Finite Difference Representation of Neutrino Radiation Hydrodynamics in Spherically Symmetric General Relativistic Spacetime. 150:263–316, Jan. 2004.

[25] M. Liebendörfer, M. Rampp, H. Janka, and A. Mezzacappa. Supernova Simulations with Boltzmann Neutrino Transport: A Comparison of Methods. *The Astrophysical Journal*, 620:840–860, Feb. 2005.

[26] M. Liebendörfer, S. C. Whitehouse, and T. Fischer. The Isotropic Diffusion Source Approximation for Supernova Neutrino Transport. *The Astrophysical Journal*, 698:1174–1190, June 2009. doi: 10.1088/0004-637X/698/2/1174.

[27] G. Martínez-Pinedo, M. Liebendörfer, and D. Frekers. Nuclear input for core-collapse models. *Nuclear Physics A*, 777:395–423, 2006.

[28] D. Mihalas and B. W. Mihalas. *Foundations of Radiation Hydrodynamics*. Dover Publications, Inc., 1999.

[29] T. Pang. *An Introduction to Computational Physics*. Cambridge University Press, 2nd edition, 2006.

[30] Y.-Z. Qian and S. E. Woosley. Nucleosynthesis in Neutrino-driven Winds. I. The Physical Conditions. *The Astrophysical Journal*, 471:331, Nov. 1996. doi: 10.1086/177973.

[31] G. Raffelt. Neutrinos and the stars. *ArXiv e-prints*, Jan. 2012.

[32] G. G. Raffelt. *Stars as laboratories for fundamental physics : the astrophysics of neutrinos, axions, and other weakly interacting particles*. 1996.

[33] S. Rosswog and M. Liebendörfer. High-resolution calculations of merging neutron stars - II. Neutrino emission. *Monthly Notices of the Royal Astronomical Society*, 342:673–689, July 2003. doi: 10.1046/j.1365-8711.2003.06579.x.

[34] M. Ruffert, H.-T. Janka, and G. Schaefer. Coalescing neutron stars - a step towards physical models. I. Hydrodynamic evolution and gravitational-wave emission. *Astronomy & Astrophysics*, 311:532–566, July 1996.

[35] M. Ruffert, H. Janka, K. Takahashi, and G. Schaefer. Coalescing neutron stars - a step towards physical models. II. Neutrino emission, neutron tori, and gamma-ray bursts. *Astromony & Astrophysics*, 319:122–153, Mar. 1997.

[36] S. E. Woosley, A. Heger, and T. A. Weaver. The evolution and explosion of massive stars. *Reviews of Modern Physics*, 74:1015–1071, 2002.

[37] H. Yasin. *Study of the neutrinosphere and electron fraction in neutrino-driven winds, jet-like supernovae and neutron star mergers*. April 2013.

List of Figures

Thanks & Appreciation

I wish to thank everyone at the Theoriezentrum at Technische Universität for being so kind, welcoming, friendly, and most of all inspiring.

I wish to thank Prof. Dr. Almudena Arcones for welcoming me into her research group and giving me the opportunity to learn so much about core-collapse supernovae. Ultimately, her understanding of my need to learn, explore and thrive was the support I was looking for. Thank you, Almudena!

I also wanted to thank my entire Arbeitsgruppe: Carlos, Dirk, Hannah, Marcella and Julia for interesting and fun conversations either over lunch or the daily Kaffeeklatsch while sharing expertise and troubleshooting advice over Python and Fortran codes. Deutsch reden mit Euch, hat echt spaß gemacht!

Last but not least, I wish to thank Dr. Albino Perego for his expertise on neutrino transport, radiation transfer, and countless sessions either in front of a chalkboard or on scratch paper. I really couldn't have understood and learned so many new things without your guidance and direction.